SAXS STUDIES OF ULTRASONICATED DISPERSIONS OF BIOMINERAL FERRIHYDRITE NANOPARTICLES USING THE ATSAS SOFTWARE PACKAGE ANALYSIS

L. Anghel[a,b], M. Balasoiu[a,c], A.V. Rogachev[a], T.S. Kurkin[d], A.I. Kuklin[a], L.A. Ishchenko[e,f], S.V. Stolyar[e,f], R.S. Iskhakov[e,f] , Yu.L. Raikher[g], G.M. Arzumanian[a]

[a]Joint Institute of Nuclear Research, Dubna, 141980, Russia
[b]Institute of Chemistry of ASM, Chisinau, Republic of Moldova
[c]Horia Hulubei National Institute of Physics and Nuclear Engineering, Bucharest, Romania
[d]Institute of Synthetic Polymer Materials RAS, 117393, Moscow, Russia
[e]Siberian Federal University, 660041, Krasnoyarsk, Russia
[f]Kirensky Institute of Physics, Siberian Branch of RAS, 660036, Krasnoyarsk, Russia
[g]Institute of Continuous Media Mechanics, Ural Branch of RAS, 614013, Perm, Russia

New methods are developing to control disparity, chemical composition, the size, and the shape to get the best particles which can be well applied in different fields of science. A promising new dimension in this field is the use of microorganisms for the production of inorganic nanoscale particles. A growing need to understand the basics of this technique to facilitate application of the new methodology to laboratory and industrial needs is present.

This paper presents SAXS studies of ultrasonicated dispersions of biomineral ferrihydrite nanoparticles produced by bacteria *Klebsiella oxytoca* using the ATSAS software package [1] analysis.

The SAXS intensity is experimentally determined as a function of the scattering vector q whose modulus is given by $q = 4\pi \sin\theta / \lambda$, 2θ is the scattering angle and λ the wavelength of the incident X-ray beam. For an ensemble of structurally homogenous, randomly oriented particles, the intensity of scattered radiation can be expressed as:

$$I(q) = N(\Delta\bar{\rho}V)^2 P(q) S(q) \quad (1)$$

In Eq. (1), N is the number of particles per unit volume; $\Delta\bar{\rho}$ is the contrast, which reflects the difference between the electronic density of the scattering components; and V is the volume of each particles; $P(q)$, the form factor, encodes the ensemble average structure of the particles in reciprocal space; and $S(q)$, the structure factor, encodes correlation distances between particles in the reciprocal space.

SAXS measurements on ferrihydrite nanoparticles were performed at the Brucker Nanostar SAXS spectrometer in function at the Institute of Synthetic Polymer Materials RAS, Moscow. The experimental setup covered the q range 0.007 – 0.23 Å^{-1}. The experimental scattering curves presented in Fig. 1, were analyzed using the software ATSAS 2.4, which is suitable for small angle scattering data analysis. In order to eliminate concentration or aggregation influence on the modeled experimental data, a linear extrapolation to zero concentration was done for the scattering data obtained on the samples with different concentrations of ferrihydrite particles. In this case, the structure factor $S(q)$ becomes equal to 1 over the whole q range, and Eq. (1) reduces to:

$$I(q) = N(\Delta\bar{\rho}V)^2 P(q) \quad (2)$$

Radius of gyration, R_G, which represents the distance of the scattering object parts from its center of gravity, was calculated in a q range of 0.024–0.034 Å^{-1} using the Guinier approximation:

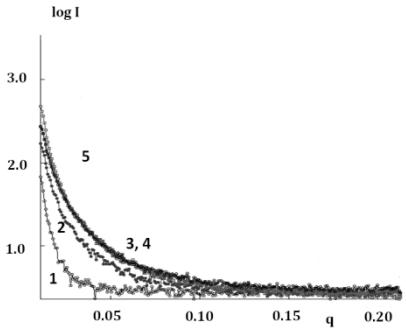

Fig.1. SAXS scattering curves from ferrihydrite samples at different concentration: buffer (1); ferrihydrite concentration 3.70×10^{-3}M (2); 5.54×10^{-3}M (3); 7.41×10^{-3}M (4); 1.48×10^{-2}M (5) plotted by PRIMUS; the logarithm of the scattering intensity $I(q)$ vs modulus of the scattering vector q is shown.

$$I(q) = I(0)\exp(-q^2R_G^2/3) \quad (3)$$

A rough value of 6.41±0.13 nm for the radius of gyration independently of the shape of the investigated particles was obtained. In order to calculate more precisely the values of R_G, the pair distribution function of biomineral nanoparticles was computed using the fitting procedures included in GNOM software from ATSAS package. Typically, the particle distance distribution function, $p(r)=\gamma(r)r^2$, where $\gamma(r)$ is the characteristic function of the particles, is calculated by an indirect Fourier transformation to avoid problems due to the discrete sampling of the $I(q)$ curve over a finite range. The indirect Fourier transform essentially constructs trial $p(r)$ functions that are Fourier transformed and evaluated in comparison with the experimental scattering. In the GNOM program, a regularizing multiplier is used to balance the smoothness of the trial $p(r)$ function with the goodness of the fit to the data. Thus, the radius of gyration is obtained from the $p(r)$ function using formula:

$$R_G^2 = \int_0^{D_{max}} r^2 p(r)dr \Big/ \int_0^{D_{max}} p(r)dr \quad (4)$$

In Eq. (4), D_{max} denotes the maximum distance inside the scattering particle. This method to determine R_G takes into accounts all of the collected experimental data, not only those limited to small q domains, as is used in the Guinier approximation. Calculated $p(r)$ distribution function in the q range 0.02 – 0.26 $Å^{-1}$ is presented in Fig. 2.

The elongated tail of the $p(r)$ function within the r - range of 120 – 200 Å indicates the presence of macromolecules in the scattering solutions. This fact, that biogenic nanoparticles removed from bacterium *Klebsiella oxytoca* are still wrapped in an organic sheath, was previously shown by HRTEM analysis. We remark also that the value of radius of gyration of 6.73±0.16 nm calculated from pair-distribution function is close to those obtained earlier from the Guinier approximation.

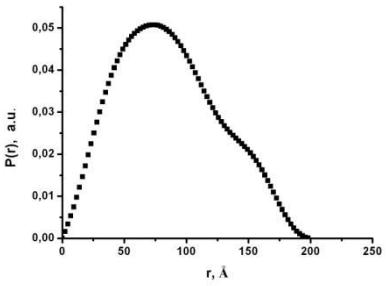

Fig.2. Function $p(r)$ calculated from the scattering curve obtained from extrapolation to zero concentration

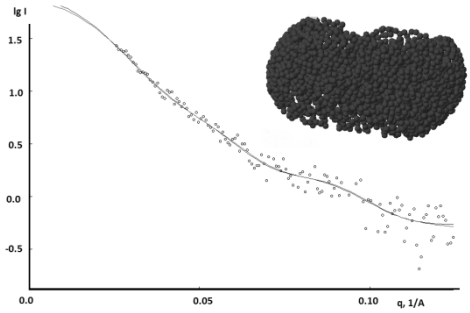

Fig.3. *ab initio* reconstruction of water dispersed ferrihydrite nanoparticles.

The overall shape of the particles was further computed by the program GASBOR. This software performs an *ab initio* reconstruction of molecular structure by a chain-like ensemble of *dummy residues*. Fig. 3 displays the resulting plot for the scattering curve obtained from a sample of biogenic ferrihydrite nanoparticles. The identified elongated 3D object resembles quite closely the rod-like model reported earlie. As any other method that generates 3D structures from the 1D scattering data, the resulting pattern is not unique and might be optimized with supplementary experimental data.

[1] D. I. Svergun, et. al. J. of Appl. Cryst. 40 (2007) s223-s228; D. I. Svergun, et. al., J. of Appl. Cryst. 25 (1992) 495-503; D. I. Svergun, et. al., Biophysical J. 80 (2001) 2946-2953

CATION DISTRIBUTION IN Zn-SUBSTITUTED Ni-Ga-Fe SPINEL

S.S. Ata-Allah[a], A.M. Balagurov[b], A. Hashhash[a], I.A. Bobrikov[b], V.G. Simkin[b], Sh. Hamdy[a]

[a] Reactor Physics Department, NRC, Atomic Energy Authority, Cairo, Egypt
[b] Frank Laboratory of Neutron Physics, JINR, Dubna, Russia

Spinels with $A^{2+}B^{3+}{}_2O_4$ formula are ternary oxides that have numerous and important technological applications, especially as magnetic, super-hard and high-temperature materials. From physical point of view, the cubic-to-tetragonal phase transformation and Jahn–Teller (JT) distortion in the tetragonal phase have attracted considerable attention during many years. For instance, the $NiFe_2O_4$ compound for the first time has been investigated by means of neutron diffraction about 60 years ago [1].

In the *normal* cubic spinel structure the oxygen ions form a cubic close packed lattice with the A and B cations occupying, respectively, tetrahedrally and octahedrally coordinated interstices. In the "*inverted*" spinel structure A- and B-cations substitute each other, which means that the real composition is $(A_{1-x}B_x)[A_xB_{2-x}]O_4$, where in parentheses and square brackets cations in A- and B-positions are shown, respectively. In general case, the inversion parameter x can be smaller than 1 (*partially inverted* spinel), but as it was shown in Ref. [2] for $NiFe_2O_4$ the degree of inversion is 1.00 and structural formula can be written as $Fe[NiFe]O_4$.

In its bulk form, $Fe[NiFe]O_4$ shows ferrimagnetic order below 850 K. Its magnetic structure consists of two antiferromagnetically coupled sublattices. A first sublattice is formed by ferromagnetically ordered Fe^{3+} ($3d^5$, magnetic moment M = 5 μ_B) ions occupying the tetragonal A sites, while the second sublattice contains ferromagnetically ordered Ni^{2+} ($3d^8$, M = 2 μ_B) and Fe^{3+} ($3d^5$, M = 5 μ_B) ions occupying the octahedral B sites. This type of ordering results in a saturation magnetization of 2 μ_B / f.u. [3].

In the Reactor and Neutron Physics Department (NRC, Cairo) the substituted spinel compounds are investigated by means of X-ray and Mössbauer techniques to shed more lights on crystallographic structure and the microscopic picture of the magnetic ordering in these diluted ferrimagnets. In particular, the Zn-substituted $Cu_{1-x}Zn_xFe_{2-y}Ga_yO_4$ compositions were investigated in details [4] and it was shown that at $x \geq 0.25$, tetragonal-to-cubic transformation occurs.

In continuation of these studies we analyze the $Ni_{0.7}Zn_{0.3}Fe_{2-y}Ga_yO_4$ compounds with y = 1.0 and 0.5. As it was determined from X-ray and magnetic measurements these compositions have cubic symmetry and the second one (y = 0.5) is ferrimagnetic. The diffraction patterns of samples S-1 (y = 1.0) and S-2 (y = 0.5) have been measured with High Resolution Fourier Diffractometer (HRFD) at the IBR-2 pulsed reactor at room, low (10 K), and high (473 K, S-2 only) temperatures. The example of raw data is shown in Fig. 1.

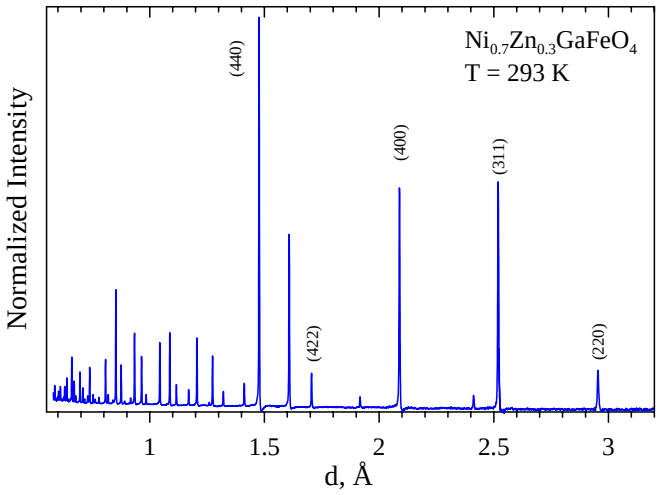

Fig 1. Diffraction pattern of the sample-1 measured with HRFD and normalized on effective neutron spectrum. Miller indices of several strong diffraction lines are indicated.

The Rietveld refinement using MRIA package was done in the frame of the Fd3m (№227) space group, the first setting (without center of symmetry). In this group the atomic positions for AB_2O_4 spinel with Z = 4 are: A in (8a), B in (16d), O in (32e) with x ≈ 3/8. The thermal factors were introduced in isotropic approximation. The next neutron scattering lengths were used in refinements: b_{Fe} = 0.954, b_{Zn} = 0.568, b_{Ga} = 0.729, b_{Ni} = 1.030, b_O = 0.581 in 10^{-12} cm units. Supposing that Fe is substituted for Zn in the A-site and all Ga atoms are in B-site it can be obtained that the coherent scattering lengths for A and B sites are: b_A = 0.838, b_B = 0.868 for S-1 and b_A = 0.838, b_B = 0.924 for S-2 again in 10^{-12} cm units.

Refinements (n_A, n_B, x_O, and B_O) of all measured patterns (an example is presented in Fig. 2) show that n_A is systematically smaller than 1 and, contrary, n_B is systematically higher than 2. The only hypothesis, which is compatible with these changes, is interchange of Fe in A-site and Ga in B-site. Numerical calculations show that in both samples around 50% of Ga atoms are shifted in the A-site. This result is important for analysis of conduction mechanism and magnetic structure of these compositions.

The magnetic contribution in the diffraction peaks is not strong but substantial. For instance, in Fig. 3 the temperature dependence of (331) line for which nuclear structure factor is close to zero is shown. The refinement of the magnetic structure is in progress now.

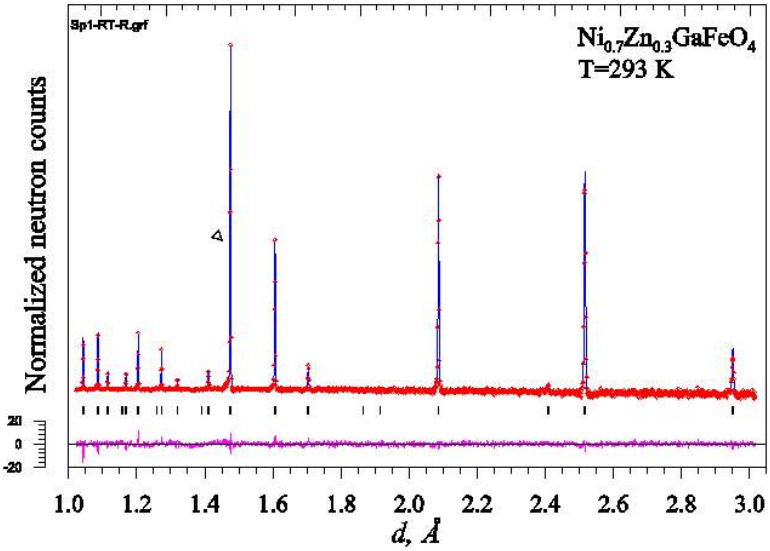

Fig. 2. Rietveld refinement of the S-1 diffraction pattern, measured at room temperature.

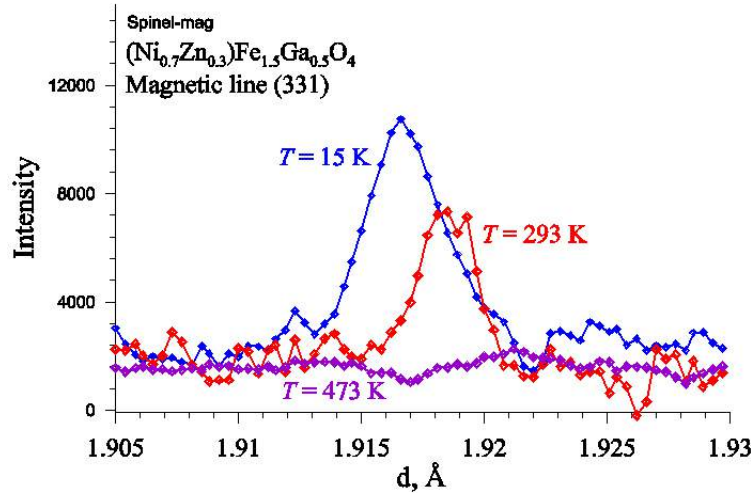

Fig. 3. Diffraction peak (331) of S-2 measured at low, room and high temperatures. Magnetic contribution is absent at 473 K.

References

[1] J.M. Hastings, L.M. Corliss, Rev. Mod. Phys. 25 (1953) 114.
[2] D. Carta et al., J. Phys. Chem. C 113 (2009) 8606.
[3] U. Luders et al., Phys. Rev. B 71 (2005) 134419.
[4] S.S. Ata-Allah, J. Solid State Chem. 177 (2004) 4443.

SANS STUDY OF BIOCOMPATIBLE MAGNETIC FLUIDS STABILIZED WITH POLY(ETHYLENE GLYCOL)

M.V. Avdeev[a], V.I. Petrenko[a,b], A.V. Nagornyi[a,b], V.M. Garamus[c], A.V. Feoktystov[d], V. Závišová[e], M. Koneracká[e], G. Lancz[e], N. Tomašovičová[e], M. Timko[e], P. Kopčanský[e]

[a]*Frank Laboratory of Neutron Physics, JINR, Dubna, Russia*
[b]*Kyiv Taras Shevchenko National University, Kyiv, Ukraine*
[c]*Helmholtz Zentrum Geesthacht, Geesthacht, Germany*
[d]*Forschungszentrum Jülich, Jülich, Germany*
[e]*Institute of Experimental Physics, Slovak Academy of Sciences, Kosice, Slovakia*

Water-based magnetic fluids have found application in a variety of fields in biotechnology and medicine (e.g. cell separations, diagnostic magnetic resonance imaging, hyperthermia, magnetic drug targeting, etc.) [1]. The coating of the nanoparticles is one of the most important factors responsible for their compatibility in the organism. The surface of ultrafine magnetic particles can be covered with molecules with different end groups. For our purpose poly(ethylene glycol) (PEG) was chosen because it is non-immunogenic, non-toxic, non-antigenic, biocompatible and soluble in water and organic solvents [2]. Highly insoluble anticancer agents can be attached to PEG, so the solubility of the modified drug will exceed that of the original drug, increasing possibility of more effective drug delivery [3]. The aim of our work was to characterize the structure of new type of biocompatible magnetic fluid prepared by surface modification with oleate and PEG for the proposed use in medicine.

The co-precipitation method of ferric and ferrous salts in an alkali aqueous medium was used to prepare spherical magnetite particles. After washing the precipitate by magnetic decantation and heating up to 50°C, the surfactant sodium oleate ($C_{17}H_{33}COONa$) was added to the mixture to prevent agglomeration of the particles. Magnetite particles stabilized by oleate bilayer were dispersed in water. Agglomerates were removed by centrifugation (9000 RPM for 30 minutes). Finally, PEG was used to improve biocompatibility of the prepared magnetic fluid. PEG with a molecular weight 1 kDa, dissolved in water, was added to magnetic fluid at 50°C at a given weight ratio PEG/Fe_3O_4. The most important ratio was 0.25 (final sample MFPEG). A magnetic fluid – magnetite particles coated with sodium oleate and PEG – was formed in this way. The PEG adsorbtion on the magnetite surface was revealed by means of attenuated total reflectance - Fourier transform infrared (ATR-FTIR) spectroscopy, as well as by differential scanning calorimetry (DSC).

The samples were studied by small-angle neutron scattering (SANS) with the contrast variation at the SANS-1 instrument, HZG, Germany. The curves were obtained in a standard way in a q-range of 0.04-2 nm^{-1}. The influence of PEG was studied in view of structuralization of magnetic particles by SANS with the contrast variation based on hydrogen-deuterium substitution in the carrier. The new approach of the modified basic functions [4], recently applied for different classes of magnetic fluids [5-9], was used with the main accent to reveal the structural information about various aggregates in the system. The initial samples were dissolved with the ratio 1:3 by different mixtures of light/heavy water, thus varying the D_2O content over the interval of 0-70 % in the final fluid. The addition of PEG to an oleate-stabilized MF may cause considerable structural changes. Large (D > 100 nm) fractal-like aggregates of individual (non-aggregated) magnetic particles with the magnetite core size of 8 nm were observed at high PEG/magnetite ratio (ca. 2.5 by mass) as opposed to compact (D < 40 nm) aggregates present without added PEG [9]. At smaller PEG/magnetite ratio of 0.25 the initial aggregates changed less significantly (Fig.1), which is an indication of only partial substitution of sodium oleate with PEG on free magnetite surface. The MFPEG of the considered PEG/Fe_3O_4 ratio was interesting because of its application in the preparation of magnetic nanospheres, which carried the anticancer drug Taxol [10]. The changes in

the scattering curves (Fig.1) were analyzed in terms of the modified basic functions $\tilde{I}_c(q)$, $\tilde{I}_s(q)$, $\tilde{I}_{cs}(q)$ [4]. The model expression:

$$I(q) = \tilde{I}_s(q) + \Delta\tilde{\rho}\tilde{I}_{cs}(q) + (\Delta\tilde{\rho})^2 \tilde{I}_c(q) \qquad (1)$$

was fitted simultaneously to all curves at different modified contrast defined as

$$\Delta\tilde{\rho} = \overline{\rho}_e - \rho_s \,, \qquad (2)$$

where $\overline{\rho}_e = \langle\rho V^2\rangle/\langle V^2\rangle$ is the averaged scattering length density (SLD), ρ, over all particles (with volume V) in the system, and ρ_s is SLD of the solvent. First, $\overline{\rho}_e$ (also called the effective match point) was found from the minimum of the forward scattering intensity (obtained by the Indirect Fourier Transform (IFT)) as a function of the D_2O content in the carrier. We were mostly interested in $\tilde{I}_c(q)$ (shown in inset to Fig. 6), which is the averaged shape scattering function taking into account the type and size polydispersity. Two regions with the features of the Guinier law can be seen in $\tilde{I}_c(q)$ and are related to compact aggregates (small q-values) and micelles of free sodium oleate (large q-values). As followed from IFT, in the spherical approximation the mean size of the aggregates was 33.0 ± 0.5 nm, while the maximal size exceeded 40 nm. Since SLDs of PEG and sodium oleate are close to that of light water, at 0 % of D_2O the scattering came mainly from magnetite. From the comparison of this scattering with $\tilde{I}_c(q)$ by the IFT treatment the difference in the maximal sizes was detected. It corresponded to the thickness of the stabilizing shell, which was estimated to be 2.0 ± 0.1 nm. The analysis of the second specific q-region gave the size of about 4 nm and concentration of above 1 vol. % for micelles of sodium oleate.

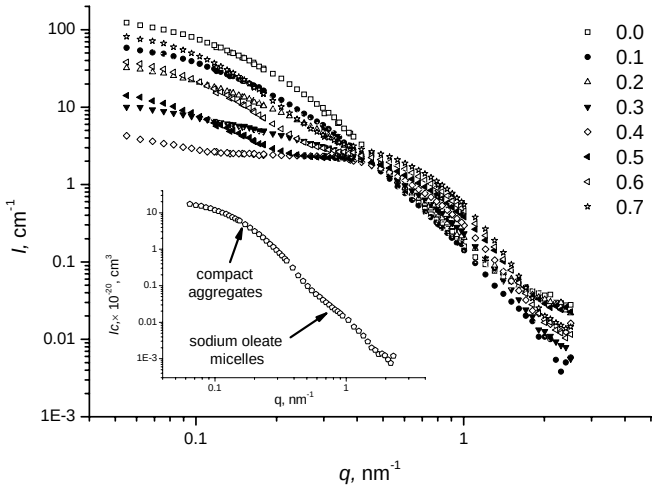

Fig 1. SANS Contrast variation of MFPEG. $I(q)$ at D_2O contents (volume fractions in solvent) from 0 to 0.7 (37°C). Inset shows the averaged shape scattering function with indicated scattering levels.

References

[1] L. Zhang, R. He, H.-Ch. Gu, Appl. Surf. Sci. 253 (2006) 2611.
[2] S. Zalipsky, C. Gilon, A. Zilkha, Eur. Polym. J. 19, 12 (1983) 1177.
[3] R.B. Greenwald, J. Controlled Release 74 (2001) 159.
[4] M.V. Avdeev, J. Appl. Cryst. 40 (2007) 56.
[5] A.V. Feoktystov, M.V. Avdeev, V.L. Aksenov, et al., Solid State Phenom. 152-153 (2009) 186.
[6] A.V. Feoktystov, M.V. Avdeev, V.L. Aksenov, et al. J. Surface Investig. X-ray Synchr. Neutron Tech. 3(1) (2009) 1.
[7] M.V. Avdeev, E. Dubois, G. Mériguet, et al., J. Appl. Cryst. 42 (2009) 1009.
[8] M.V. Avdeev, B. Mucha, K. Lamszus, et al., Langmuir 26 (2010) 8503.
[9] M.V.Avdeev, A.V. Feoktystov, P. Kopčanský, et al., J. Appl. Cryst. 43 (2010) 959.
[10] V. Závišová, M. Koneracká, M. Múčková, et al., J. Magn. Magn. Mater. 321 (2009) 1613.

MAGNETIC FIELD AND PARTICLE CONCENTRATION COMPETITIVE EFFECTS ON FERROFLUID BASED SILICONE ELASTOMER MICROSTRUCTURE

M. Balasoiu[a,e], I. Bica[b], V.T. Lebedev[c], A.I. Kuklin[a], Yu.L. Raikher[d]

[a]Joint Institute of Nuclear Research, Dubna, Russia
[b]West University of Timisoara, Department of Electricity and Magnetism, Timisoara, Romania
[c]Petersburg Nuclear Physics Institute, Gatchina, Russia
[d]Institute of Continuum Media Mechanics, Ural Branch of RAS, Perm, Russia
[e]National Institute of Physics and Nuclear Engineering, Bucharest, Romania

The study of the properties of filled elastomers is a challenging and exciting topic for both fundamental science and industrial application. It is know that the addition of hard particulates to a soft elastomer matrix results in properties that do not follow a straightforward rule of mixtures. The progress of structure-properties relationships research for such systems evolves into several directions: filler type and structure, magneto(electro) - hydrodynamic reinforcement and interactions between fillers and elastomers. Development of novel technologies of magnetic nanomaterials shows the trends of the creation of composites with anisotropic molecular and magnetic structures such as elastomers filled with tiny ferroparticles. The combination of polymers with magnetic materials displays new and often enhanced properties. The magnetic particles couple the shape of the elastomer to the external magnetic field. Combination of the magnetic and the elastic properties leads to a number of striking phenomena that are exhibited in response to impressed magnetic field [1]. The synthesis and the study of structure and physical properties of these advanced materials combining the functional properties of elastic polymers and ferromagnetic substances should be considered as a perspective way to provide the understanding of construction principles of a wide class of materials for electronics, electrical engineering, medicine, aero- and cosmic industries. Also from the fundamental point of view it is needed a comprehensive analysis of the relationship between macromolecular and disperse phase structures and their ordering under the action of magnetic field and by the variation of magnetic component content. Neutron and X-ray scattering techniques are highly useful for determining the morphology of the formed filler structures [2-4].

The aim of present work is the small-angle neutron scattering examination of subtle structural features of polymeric matrix and ensemble of embedded ferroparticles as resulted from the conditions of preparation of ferroelastomers by the variation of concentration of ferroparticles and strength of the external applied magnetic field during the polymerization.

Ferroelastomers were prepared using the radical polymerization of dimetylsiloxane with addition of ferrofluid based on magnetite. In the samples the concentration of magnetic component (ferrofluid) was varied: 1.27; 3.9; 5.88 % mass. The magnetic field (B = 0; 280; 560; 1120 Gauss) was applied perpendicular to the plane of polymeric film (thickness of ~ 0.5 mm) (Table 1). It was prepared also the polymeric matrix without ferroparticles (reference sample).

The small-angle neutron scattering experiments (SANS) have been carried out at ambient temperature (20^oC) on the diffractometer "Membrane" (PNPI) in the range of momentum transfer $q = (4\pi/\lambda)\sin(\theta/2) = 0.03\text{-}0.8\ nm^{-1}$, where θ is scattering angle and $\lambda = 0.3$ nm is neutron wavelength ($\Delta\lambda/\lambda = 0.25$).

The scattering patterns for the elastomers containing 5.88; 3.9 and 1.27 % mass of magnetite are presented in Figure 1(a-c) where the data for the matrix are shown also. It is evident (Figure 1) that the scattering from original polymeric matrix is relatively strong at $q \leq 0.2\ nm^{-1}$. The addition of ferroparticles into matrix does not provide any substantial contribution to the total scattering intensity at low momenta even at high concentration of magnetite (5.88 % mass.). The scattering from ferroparticles dominates only at larger momenta, $q \geq 0.4\ nm^{-1}$ due to their small size as compared to inhomogeneities in polymer matrix. It should be noted that the

application of magnetic field (B = 1120 Gs, sample P_{15}) during the polymerization did not initiate any dramatic structural changes. It is observed a moderate increase in scattering: the ratio of intensities for samples P_{15} (strong field) and P_{12} (no field) does not exceed factor 2 in the interval of q = 0.4-0.8 nm^{-1}. This means that the polymer network prevents the aggregation of ferroparticles and provides their more homogeneous spatial distribution to be achieved for required material quality. Large-scale inhomogeneities in polymer matrix are visible despite of low scattering ability of polymer having the density of coherent length $K_S = 6.3 \cdot 10^8$ cm^{-2}. It is by 2 orders in magnitude lower than that for magnetite having $K_M = 6.971 \cdot 10^{10}$ cm^{-2}. Thus, the contrast factor for magnetite regarding to matrix is also high, $\Delta K_M = K_M - K_S = 6.91 \cdot 10^{10}$ $см^{-2}$, but it is compensated by small characteristic volume of a particle as compared to large inhomogeneities in matrix, as it is seen in Figure 1b and Figure 1c.

A detailed analysis of q-dependencies of scattering intensity for matrix enables us to built the two-level model structure and related scattering function

$$I(q) = I_{01} \exp[-(qR_g)^2 / 3] + I_{02}[1 + (qR_c)^2]^{-2} \qquad (1)$$

The first Guinier-term describes the large scale inhomogeneities (domains, radius gyration R_G), and the second Debye-term is related to the smaller globular objects (domains) with correlation radius R_C.

For ferroelastomers we have used the model (2) taking into account the scattering from large-scale polymer domains (gyration radius R_G) and ferroparticles (correlation radius r_C) separated in space at the distance L comparable to small polymer domain diameter ~ $2R_C$:

$$I(q) = I_{01} \exp[-(qR_g)^2 / 3] + I_{02}[1 + (qR_c)^2]^{-2}[1 + n \sin(qL)/(qL)] \qquad (2)$$

In expression (2) the parameters I_{o1}, I_{o2} represent the contributions of large polymer domains and ferroparticles in scattered intensity at q $\rightarrow$0. The value of n is the average number of particles correlated with a given particle at the characteristic distance L. The function (2) describes satisfactory the behaviors of scattering intensities for ferroelastomers at all the concentrations and the magnitudes of induction B.

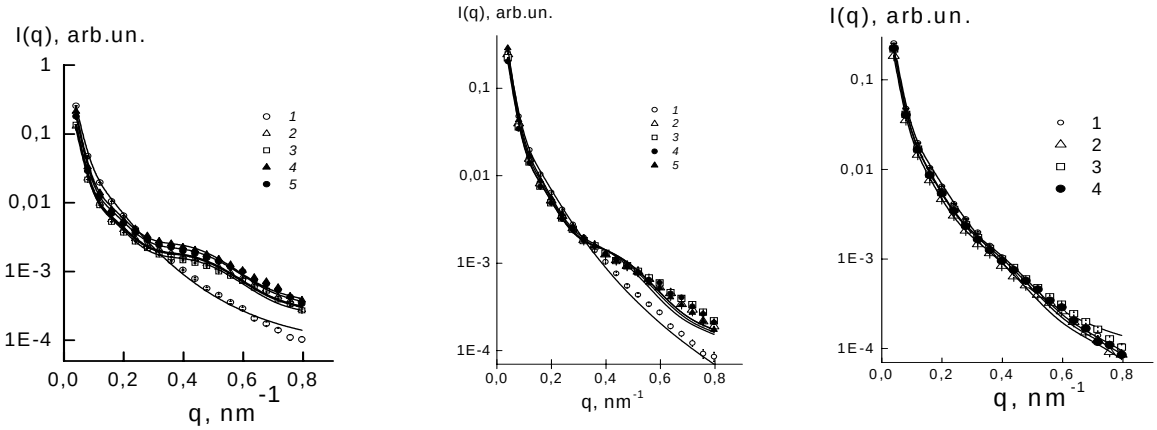

a) b) c)

Figure 1. Scattering intensities I(q) vs momentum transfer q for matrix P_1 (1) and ferroelastomers P_{12}-P_{15} (2-5) with high content of magnetite (a); ferroelastomers P_{21}-P_{25} (2-5) with moderate content of magnetite (b); ferroelastomers P_{32}, P_{33}, P_{35} (2-4) with low content of magnetite (c) (synthesis in magnetic field perpendicular to the plane of polymer film). Lines are the approximation functions (1) and (2) for matrix and ferroelastomers.

References

[1] Stolbov O V, Raikher Yu L, Balasoiu M 2011 *Soft Matter* **7** 8484

[2] Balasoiu M, Craus M L, Anitas E M, Bica I, Plestil J and Kuklin A I 2010 *Phys.Solid State* **52(5)** 917

[3] Balasoiu M, Bica I, Raikher Yu L, Dokukin E B, Almasy L, Vatzulik B, Kuklin A I 2011 *Optoelectron. Adv. Mater. – RC* **5(5)** 523

[4] Balasoiu M, Lebedev V T, Orlova D N, Bica I 2011 *Crystallogr. Rep.* **56(7)** 1177

NEUTRON DIFFRACTION STUDY OF $LiFePO_4$ CATHODE MATERIAL DOPED WITH VANADIUM OXIDE

I.A. Bobrikov[a], V.G. Simkin[a], Chih-Hao Lee[b], Chi-Wei Hu[b], Tsan-Yao Chen[b], Sangaa Deleg[a], A.M. Balagurov[a]

[a] *Frank Laboratory of Neutron Physics, JINR, Dubna, Russia*
[b] *Dept. Engineering and System Science, National Tsing-Hua Univ., Hsinchu, Taiwan*

$LiFePO_4$ (LFP) is one of the most promising cathode materials for the next generation of lithium-ion battery because its appealing electrochemical features including excellent chemical/thermal stability, low material cost, non-toxicity, and a high theoretical capacity. However, the poor ionic as well as electrical conductivity and the incomplete utilization of capacity are fatal defects significantly hinders its applications. In studies performed by Liu *et al*. [1] it was found that the doping of a heteroatom (Ti, Zr, V, Nb, and W) could promotes the performance of $LiFePO_4$ at high current due to the enlarged lattice volume that provides more space for lithium-ion transfer. Meanwhile, Jint *et al*. [2] found that introduction of a small amount of vanadium into the carbon-coated LFP particles would significantly improves the rate capability and low-temperature performance due to the formation of conductive V_2O_3 nano-grains. Thus, to probe the crystal evolutions of materials upon varying charge and discharge conditions is of essential importance in terms of depicting the effects of VO on Li trajectories in LFP.

By applying high resolution neutron diffraction, we anticipate depicting the structure evolution of x·VO doped LFP samples as a function of temperature. As the first step, two samples of VO doped LFP with x = 0 and 0.0075 have been measured with HRFD instrument at the IBR-2 pulsed reactor at room and low temperature. The last measurement has been performed to elucidate the magnetic structure of the compound, which is known as antiferromagnetic below $T_N \approx 52$ K [3]. Neutron diffraction patterns have been measured by several detectors: high-resolution back-scattering (up to 3.7 Å), low-resolution (up to 4.5 Å), and PSD at 2θ = 15° (up to 16 Å). Example of the high-resolution patterns is shown in Fig. 1.

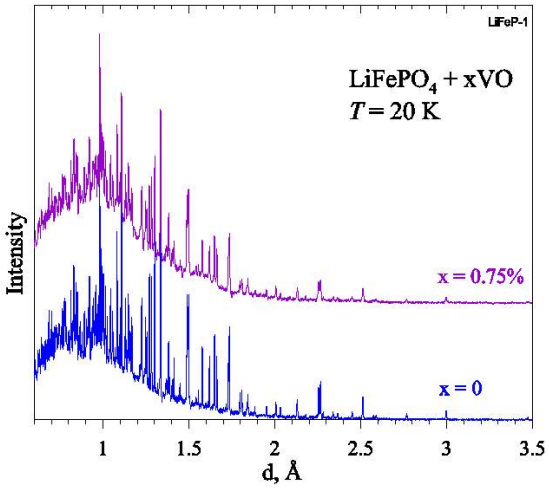

Fig 1. Diffraction pattern of the x = 0 and 0.75% samples measured with HRFD at low temperature.

The Rietveld refinement using MRIA package [4] was performed in *Pnma* (№62) space group with the model from Ref. [3]. In this group the atomic positions for perovskite structure with Z = 4 are: Li in (4a) (0,0,0), Fe, P, O1, and O2 in (4c) (x,1/4,z), O3 in (8d) (x,y,z). The thermal factors were introduced in isotropic approximation. The following values of neutron scattering lengths were used in refinements: b_{Li} = -0.222, b_{Fe} = 0.954, b_P = 0.513, b_O = 0.581 in 10^{-12} cm units. Examples of refinement are presented in Fig. 2.

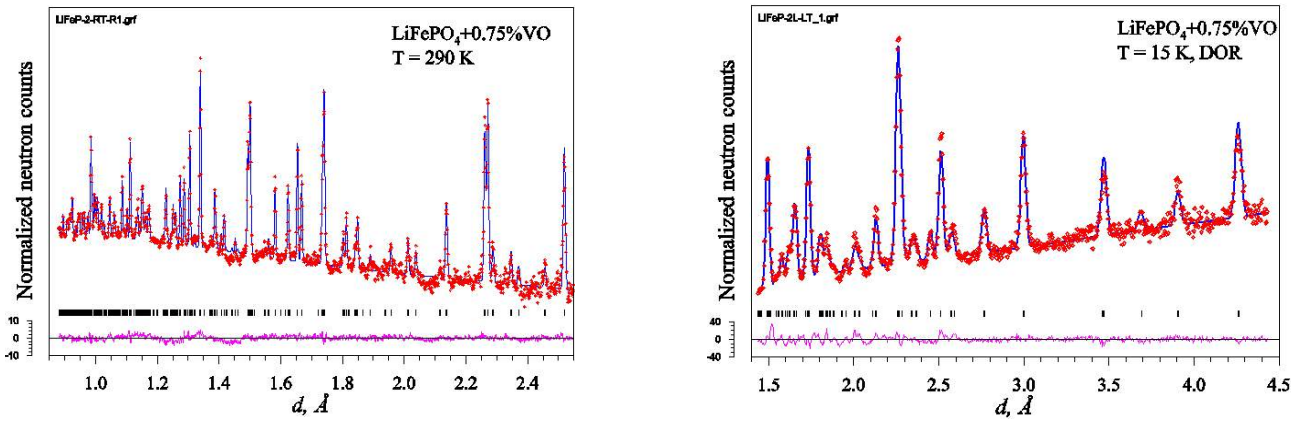

Fig 2. Rietveld refinement of the diffraction pattern (x = 0.75%), measured with high-resolution at room temperature (on the left) and low-resolution at low temperature (on the right). At this stage of refinement no magnetic phase has been introduced. There are some irregularities in the background, which reflect structural disorder at local level.

The refined atomic coordinates are in very good agreement with G. Rousse *et al.* [3] data. Moreover, the atomic coordinates are practically the same for both samples and both temperatures – the maximal changes in atomic bonds is around 0.03 Å. It means that there is no noticeable structural transformation during temperature lowering and owing to introducing of VO. The only marked difference between two samples is in level of microstrains in crystallites: they are at the conventional level for the x = 0 sample and are 1.5 higher for the x = 0.75% sample. For further analysis it would be useful to measure diffraction peaks width dependences for several VO contents.

No additional reflexions appear at temperature lowering, though intensities of several peaks increase markedly, namely, of (101), (210), and (301) peaks, which indicates that the magnetic structure corresponds to the propagation vector **k** = 0. The refinement in the frame of model from Ref. [3] shows good agreement between experimental and calculated magnetic intensities. Temperature scan has been performed and the Neel temperature has been obtained as $T_N \approx 50$ K from ratio (101) and (211) intensities (Fig. 3).

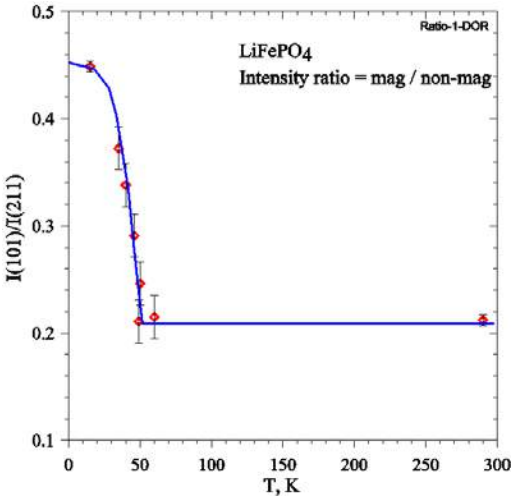

Fig. 3. Ratio of intensities of "magnetic" (101) and "non-magnetic" (211) peaks (x = 0 sample) as a function of temperature. The Neel temperature is close to 50 K.

References

[1] H Liu *et al.*, J. Solid State Electrochem. **12** (2008) 1017.
[2] Y. Jint *et al.*, J. Power Sources **196** (2011) 5623.
[3] G. Rousse *et al.*, Chem. Mater., **15** (2003) 4082.
[4] V.B. Zlokazov, V.V. Chernyshev, J. Appl. Cryst. **25** (1992) 447.

NEUTRON DIFFRACTION STUDY OF ATOMIC AND MAGNETIC STRUCTURES OF $La_{1-x}Sr_xFe_{2/3}Mo_{1/3}O_3$

I.A. Bobrikov[a], V.G. Simkin[a], S.Ya. Istomin[b], V.V. Vishnyakova[b], M.V. Lobanov[b], E.V. Antipov[b], A.M. Balagurov[a]

[a] *Frank Laboratory of Neutron Physics, JINR, Dubna, Russia*

[b] *Department of Chemistry, Moscow State University, Moscow, Russia*

The $LaFe_{2/3}Mo_{1/3}O_3$ (LFM) perovskite like compound has been synthesized for the first time and characterized in 1996 [1]. X-ray data shows that it is crystallized in the *Pnma* space group ($GdFeO_3$ structural type) without any order in the B-sites. The compound is antiferromagnetic below T_N = 520 K, but exact type of magnetic structure was unknown so far. Its electrical conductivity is high enough (1.5 Ω*cm at 25°C) for considering LFMO as potential electrode material for SOFC.

Under La → Sr substitution the unit cell parameters are changed as typical for solid solutions. According to X-ray diffraction results the atomic structure of $La_{1-x}Sr_xFe_{2/3}Mo_{1/3}O_3$ is stable up to x = 0.67. No additional diffraction lines appear which can be attributed to Fe/Mo ordering. Structure refinement is hampered due to "pseudocubic" lattice symmetry: resolution of conventional X-ray laboratory equipment is not enough to see clearly orthorhombic splitting. The Neel temperature depends on Sr content and reaches ~700 K for x = 0.5.

To refine atomic and magnetic structures of Sr-substituted LFM neutron diffraction patterns for x = 0.3 (at 20°C и 350°C) and 0.5 (at 20°C and 450°C) samples have been measured at HRFD diffractometer at the IBR-2 reactor in Dubna. Several detectors were used for data acquisition: high-resolution back-scattering (up to 3.7 Å), low-resolution (up to 4.5 Å), and PSD at 2θ = 30° (up to 16 Å). Example of the high-resolution patterns is shown in Fig. 1.

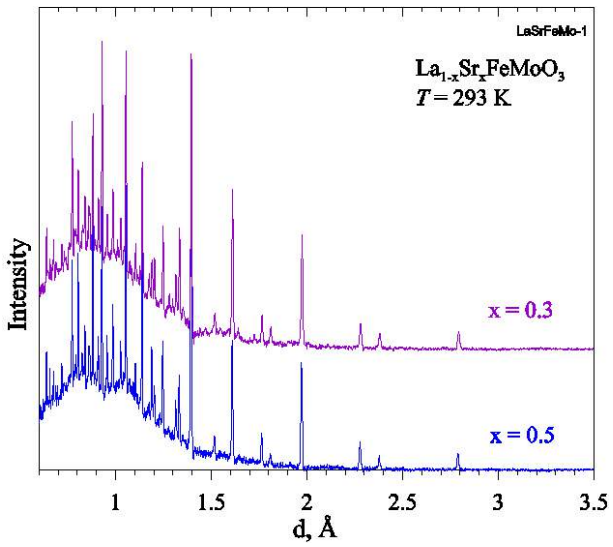

Fig 1. Diffraction pattern of the x = 0.3 and 0.5 samples measured with HRFD at room temperature.

At high temperature intensity of some diffraction lines strongly reduces, as it is seen in Fig. 2, which is connected with vanishing of AFM order. For both samples all peaks can be indexed with *Pnma* space group in the standard setting: $a \approx c \approx \sqrt{2}a_c$, $b \approx 2a_c$, where $a_c \approx 3.9$ Å is the parameter for the ideal cubic perovskite.

The Rietveld refinement using MRIA package [2] was performed in *Pnma* (№62) space group. In this group the atomic positions for perovskite structure with Z = 4 are: (La/Sr) (4c) (x,1/4,z), (Fe/Mo) (4b) (0,0,1/2), O1 (4c) (x,1/4,z), and O2 (8d) (x,y,z). The thermal factors were introduced in isotropic approximation. The following values of neutron scattering lengths were used in refinements: b_{La} = 0.824, b_{Sr} = 0.702, b_{Fe} = 0.954, b_{Mo} = 0.672, b_O = 0.581 in 10^{-12} cm units.

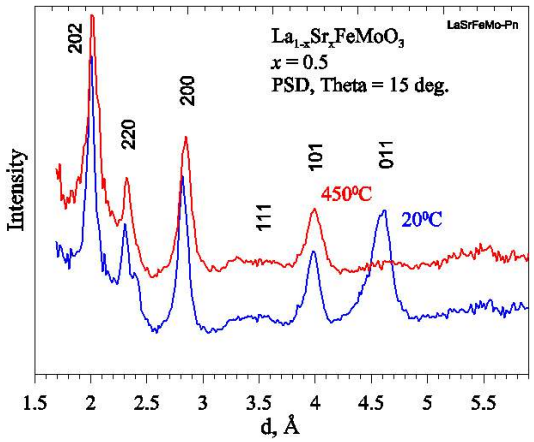

Fig 2. Diffraction pattern of the x = 0.5 sample measured with PSD at room and high temperatures. At T = 450°C the (011) peak at d ≈ 4.6 Å is practically absent.

Refinements of structural parameters of both samples (an example is presented in Fig. 3) show that LSFM has typical orthorhombically distorted perovskite structure. The special features are slightly modulated incoherent background, which can be connected with correlative disorder, and quite large width of diffraction peaks. Supposing that the second effect is connected with microstresses in crystalline grains they can be estimated as $\Delta a/a \approx 0.004$ at room and 0.008 at high temperatures. For conventional orthorhombic perovskites $\Delta a/a$ is of order 0.002, which means that for LSFM the microstresses are approximately 2 times larger and become twice more at high temperature.

The magnetic structure was solved as G-type, according to the classification of Ref. [3], with **k** = 0: magnetic moments of neighboring Fe atoms have opposite directions. For such model the first diffraction peaks with strong magnetic contribution are (011) (4.56 Å), [(112), (211), (031), (≈ 2.38 Å), [(013), (132), (231), (≈ 1.81 Å). Intensity of just these peaks strongly reduced at high temperature. Because of strong diffraction peaks overlapping the direction of magnetic moment can not be reliably determined. The refinement of the magnetic moment value will be performed later.

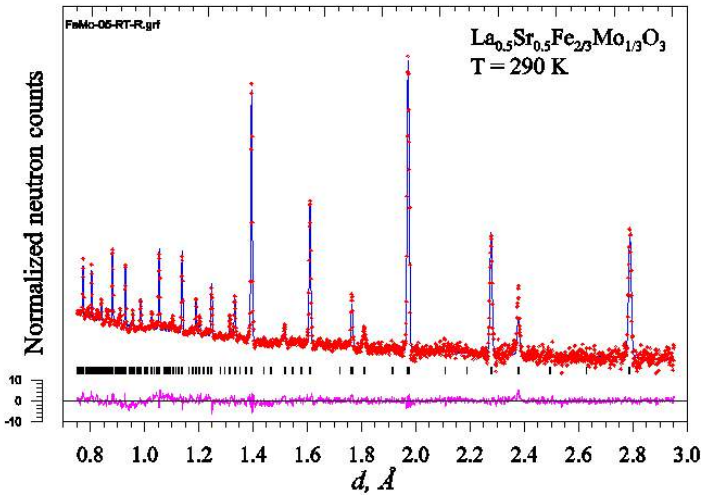

Fig. 3. Rietveld refinement of the diffraction pattern (x = 0.5), measured at room temperature. At this stage of refinement no magnetic phase has been introduced.

References

[1] G.V. Bazuev, V.G. Zubkov, G.P. Shvejkin, J. Inorganic Chem. **41** (1996) 2000.
[2] V.B. Zlokazov, V.V. Chernyshev, J. Appl. Cryst. **25** (1992) 447.
[3] E.O. Wollan, W.C. Koehler, Phys. Rev. **100** (1955) 545.

THE STRUCTURAL STUDIES OF ANTIFERROELECTRIC-FERROELECTRIC PHASE TRANSITION IN SODIUM NIOBATE.

S.G. Jabarov[a,b], D.P. Kozlenko[a], S.E. Kichanov[a], A.I. Mamedov[b], B.N. Savenko[a], R.Z. Mextieva[b] and C. Lathe[c]

[a]Frank Laboratory of Neutron Physics, JINR, 141980 Dubna, Russia
[b]Institute of Physics, Azerbaijan National Academy of Sciences, AZ 1143, Baku, Azerbaijan
[c]Helmholtz Centre Potsdam, Telegrafenberg , 14473 Potsdam, Germany

The perovskite ferroelectric materials have been extensively studied during last years due to fundamental interest and technological applications [1]. In this class of materials, lead-free alkaline niobates: $KNbO_3$, $LiNbO_3$ and $NaNbO_3$ have high piezoresponse comparable to classical PZT ceramics. One of the members, $NaNbO_3$ is a well-documented antiferroelectric which finds applications in high density optical storage, enhancing non-linear optical properties, as hologram recording materials, etc [1, 2].

At ambient conditions the sodium niobate is antiferroelectric. At low temperature a ferroelectric phase with rhombohedral symmetry occurs below 190 K [3] in $NaNbO_3$. The phase transition from antiferroelectric to ferroelectric is associated with a small tilt of the NbO_6 octahedron [4]. The structure futures of antiferroelectic and ferroelectric phases and primary mechanisms of such phase transition remain unexplored. The knowledge of relationship between ferroelectric or antiferroelectric states and crystal structure features, which can be derived from high pressure investigations, is very essential for understanding the nature of physical phenomena observed in sodium niobate.

We have studied the structure changes in $NaNbO_3$ by means of energy-dispersive X-ray diffraction at high pressure up to 4.0 GPa. The X-ray diffraction experiments were carried out using the multianvil X-ray system MAX80 at F2.1 beamline of storage ring DORIS-III. The sample was placed in the cylindrical boron nitride container with an internal diameter of 1 mm. The upper half was filled with the sample, the lower half contained sodium chloride powder for pressure calibration. The cubic boron-epoxy chamber with sample container was compressed by six tungsten carbide anvils in a large hydraulic press. The temperature at the sample was produced by an internal graphite heater and controlled by thermocouples. Diffraction patterns were recorded in an energy dispersive mode using white synchrotron X-rays from the storage ring DORIS-III. The incident X-ray beam was collimated to 100 × 100 μm with a divergence smaller than 0.3 mrad. Spectra were recorded by a Ge solid-state detector with a resolution of 153 eV at 5.9 keV resulting in a resolution of diffraction patterns of $\Delta d/d \approx 1\%$. The Bragg angle 2θ was fixed at 9.093°, counting times for each diffraction pattern were about 4 min.

At pressure P=1.6 GPa the significant changes in pressure dependences of diffraction peaks position and its width were observed. Those changes are corresponding to the phase transition from antiferroelectric to ferroelectric phase in sodium niobate. The pressure dependence of the lattice parameters and unit cell volume of both phases are shown in Fig. 1.

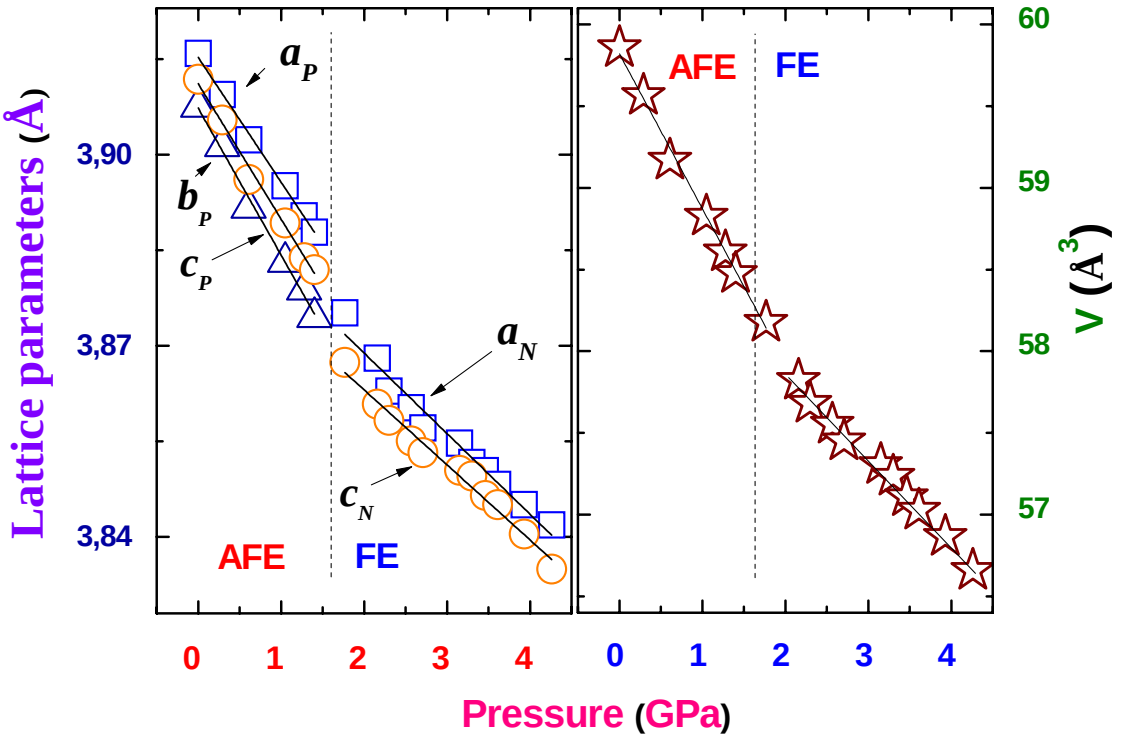

Figure 1. *The pressure dependencies of unit cell parameters and volume of the rhombohedral ferroelectric FE (a_N and c_N) and orthorhombic antiferroelectric AFE (a_P, b_P and c_P) phases of sodium niobate.*

The linear compressibility $k_i = -(1/a_{i0})(da_i/dP)_T$ ($a_i = a, b, c$) of unit cell parameters are k_a = 0.0050(6), k_b = 0.0071(7), k_c = 0.0054 (5) GPa^{-1} for the orthorhombic antiferroelectric phase and k_a = 0.0032(8), k_c = 0.0042(5) GPa^{-1} for the rhombohedral ferroelectric phase.

The pressure dependence of unit cell volume was approximated by the Birch-Murnaghan equation of state [6]. The calculated values are B_0 = 37(3) GPa and B' = 4(1) for the antiferroelectic phase and B_0 = 45(3) GPa, B' = 4(1) for the ferroelectric phase of sodium niobate.

[1] Cross E., Nature., V.432. P.24 (2004).
[2] Falcao-Filho E.L., Bosco C.A.C., Maciel G.S., et al., Phys. Rev. B., V.69. P.134204 (2004).
[3] Tripathi S., Pandey D., Mishra S.K. et al., Phys. Rev. B, V.**77.** P.052104 (2008).
[4] Yuzyuk Yu.I., Simon P., Gagarina E. et al., J. Phys.: Condens. Matter, V.17. P.4977 (2005).
[5] Ahtee M., Glazer A.M., Megaw H.D., Philos. Mag., V.26. P.995 (2005).
[6] Birch F. J., J. Geophys. Res. 91, 4949 (1986).

THE STRUCTURAL STUDIES OF $Y_3Al_5O_{12}:Ce^{3+}/Lu_2O_3$ PHOSPHORS SYNTHESIZED BY COLLOID-CHEMICAL METHOD.

S.E. Kichanov[a], E.V.Frolova[b], G.P.Shevchenko[b], D.P.Kozlenko[a], A.V.Belushkin[a], E.V.Lukin[a], G.E.Malashkevich[c], S.K.Rakhmanov[b], V.P.Glazkov[d] and B.N.Savenko[a]

[a]Frank Laboratory of Neutron Physics, JINR, 141980 Dubna, Russia
[b]Research Institute for Physical Chemical Problems of the BSU, 220080, Minsk, Belarus
[c]B. I. Stepanov Institute of Physics the Belarusian Academy of Sciences, 220072 Minsk, Belarus
[d]Russian Research Center "Kurchatov Insitute", 123182, Moscow, Russia

At the present time one of the topical problems in optics is a search for phosphors, which under excitation with light could efficiently radiate energy in a given spectrum range with minimal losses [1]. The promising materials are crystalline systems based on yttrium aluminum garnet $Y_3Al_5O_{12}$ (YAG). For example, neodymium-doped YAG:Nd^{3+} is a well-known laser material, but cerium-doped yttrium garnet $Y_3Al_5O_{12}:Ce^{3+}$ is used in several applications such as solid-state lighting, displays, scintillators [2]. The Ce^{3+} ion is responsible for nanosecond decay time and an intense yellow-green emission wavelength. So it are suitable yellow-emitting phosphors for the application to white light-emission diodes - LEDs [3].

The physical and optical properties of $Y_3Al_5O_{12}:Ce^{3+}$ depend on crystal structure features. YAG:Ce^{3+} has the cubic garnet crystal structure with a lattice parameter a=12.011(3) Å. In garnet structure, there are 24 dodecahedral sites, 16 octahedral sites, and 24 tetrahedral sites.

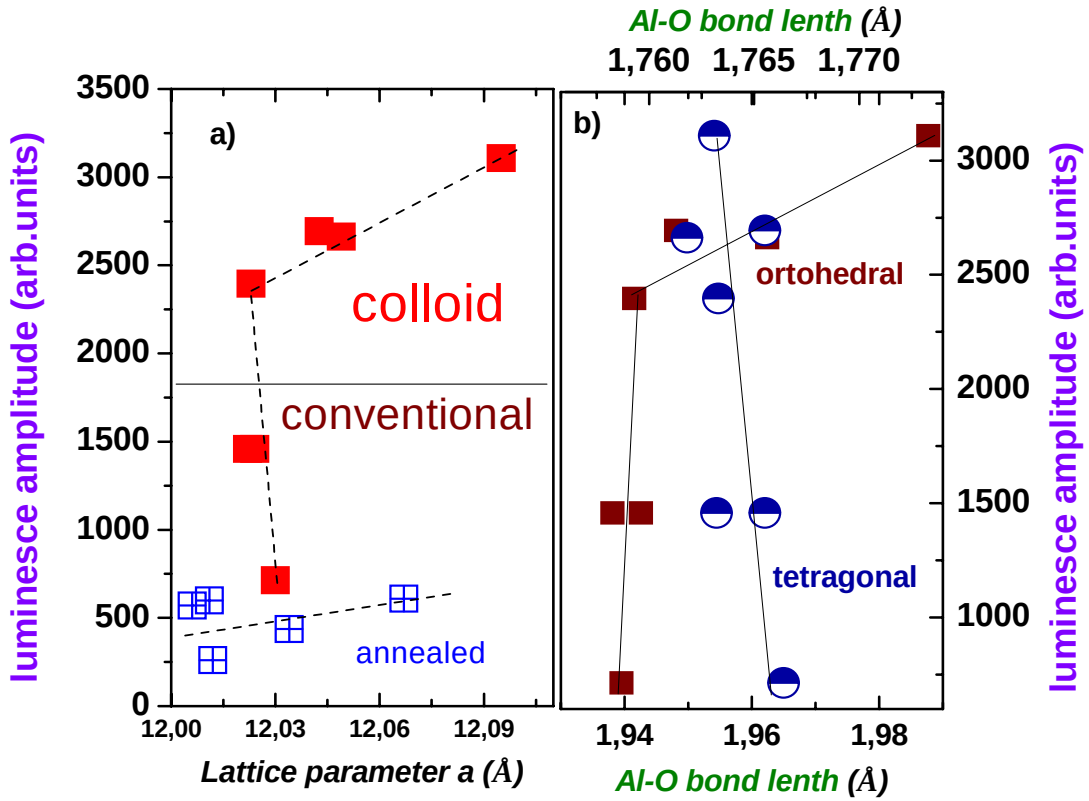

Figure 1. a) *The total luminescent intensity as function of lattice parameter of phosphors YAG:Ce^{3+}/Lu_2O_3, obtained colloid-chemical and conventional methods. The red symbols are corresponded by initial sample and blue ones with annealed samples.* ***b)*** *The total luminescent intensity as function of Al-O bonds in tetragonal and octahedral oxygen environment.*

The optical properties of such phosphors are strongly depends of crystal parameters as bond lengths and valence angles due metastable defect structure forming. The chemical-colloid methods of oxide system synthesis [4] to allow tuning of such defect structure and vacancies concentration and, as result, the optical properties of garnet-based phosphors.

Our optical measurements of $Y_3Al_5O_{12}:Ce^{3+}$ have been shown, that way of Ce^{3+} doping via additional insertion of Lu_2O_3 oxide, can be drastically improve light emission intensity of those phosphors. For structural aspects of this effect studies the neutron diffraction experiments have been prepared.

Neutron diffraction measurements at ambient conditions were performed with the DISK diffractometer at the IR-8 reactor, Moscow, Russia. The sample with a volume about 25 mm^3 was placed in vanadium container. The typical exposition time for each pressure point was to 20 h.

The lattice parameters and bond lengths have been calculated from obtained neutron data. It was found that yttrium aluminum garnets, obtained by colloid-chemical methods are characterized by greater lattice parameter (Fig. 1a) and longer length of Al-O bond in octahedral oxygen coordination (Fig. 1b). As result, the total luminescent intensity of those compounds is drastically higher than for compound obtained by conventional chemical method (Fig.1a). So difference in lattice parameters and bond lengths is result of forming stable defect substructure in oxygen lattice [4]. It was found such defect substructure formed in octahedral coordination environment of aluminum (Fig. 1b). The defect substructure in oxygen lattice have been broken by additional annealing of compounds, and as result the enhanced luminescence intensity was suppressed to intensity level observed for yttrium aluminum garnets, obtained by conventional methods (Fig. 1a).

[1] H. Chandler. Mater.Sci.Eng.R., 49, 113-155 (2005).

[2] S.W. Allison, J.R. Buczyna, R.A. Hansel, D.G. Walker, G.T. Gillies, J. App. Phys., 105(3), 036105 (2009).

[3] M. Globus, B. Grinyov, Inorganic Scintillators for Modern and Traditional Applications. –Kharkiv, 2005.

[4] E.V. Frolova, M.I. Ivanovskaya, Structural defects formation in the inorganic sol-gel derived oxides in thesis book of Defect and Diffusion Forum. Annual Retrospective VII. Switzerland: Trans. Tech. Publ., 242–244, 143–158 (2005).

EXPERIMENTAL DETERMINATION OF NEUTRON CHANNELING LENGH IN PLANAR WAVEGUIDE

S.V. Kozhevnikov[a], F. Ott[b,c], A. Rühm[d], and J. Major[d]

[a]*Frank Laboratory of Neutron Physics, JINR, 141980 Dubna Moscow Region, Russian Federation*
[b]*CEA, IRAMIS, Laboratoire Léon Brillouin, F-91191 Gif sur Yvette, France*
[c]*CNRS, IRAMIS, Laboratoire Léon Brillouin, F-91191 Gif sur Yvette, France*
[d]*Max-Planck-Institut für Intelligente Systeme (formerly Max-Planck-Institut für Metallforschung), Heisenbergstr. 3, D-70569 Stuttgart, Germany*

Neutron planar waveguide transforms the conventional neutron beam into a very narrow (about 0.1 μm width) and slightly divergent (about 0.1°) microbeam. Such narrow beam can be used for investigation of nanostructures with submicron space resolution. In [1] non-polarized microbeam was demonstrated experimentally. In our experiment [2] magnetic waveguides were investigated and polarized neutron microbeam was demonstrated.

Neutron wave function is resonantly enhanced inside a guiding layer (channel) and neutron channeling phenomenon takes place. A decay length of a neutron wave in the channel along the interfaces is an important parameter of waveguides. The theory of neutron channeling in planar waveguides can be found in [3]. Experimentally neutron channeling phenomenon was observed in [4-7]. But the channeling length was not measured experimentally. We report experimental results on direct measurement of the neutron channeling length in planar waveguide.

The measurements were done at the polarized neutron reflectometer N-ReX$^+$ (reactor FRM II, Garching, Germany). The fixed neutron wavelength 0.426 nm (1 % FWHM) was used. The angular divergence of the primary beam was 0.006°. The sample Fe(20 nm)/Cu(140 nm)/Fe(50nm)//*glass* (substrate) was investigated [3]. The sample sizes were 30×30×5(substrate) mm^3. The polarized neutron beam (+) was used. The scheme of experiment is shown in Fig. 1. The incidence angle of the primary beam is α_i. The primary beam tunnels through the upper layer with the thickness a into the guiding layer with the thickness d. Then neutrons channel at the resonance condition in the guiding layer and the neutron microbeam leaves the edge under Fraunhofer diffraction conditions. We measure the intensity of the outgoing microbeam $I(x) = I(0) \cdot \exp(-x / x_e)$ as a function of the length x of the absorbing Gd_2O_3 powder on the sample surface. Here $I(0)$ is the measured intensity of the microbeam without the Gd_2O_3 powder (x = 0) and x_e is the channeling length to be defined.

In Fig. 2a the integrated (over the incidence angle interval at resonance n=0 and the diffraction angle interval $\Delta\alpha_f = \pm 0.1°$) intensity of the microbeam is shown. Fit by exponential function gives the channeling length $x_e = 3.2 \pm 0.5$ mm. In Fig. 2b this dependence is shown in natural logarithm scale. One can see that the experimental points are described by the straight line within statistical errors which gives the error of the defined channeling length. From the theory, the channeling length increases with an increasing of the thickness a of an upper layer and the thickness d of a guiding layer. The channeling length also depends on optical potentials of the layers of waveguides. The channeling length calculated from the theory for the incident angle of the resonance α_{i0}=0.37° is equal to x_e = 3.5 mm. Thus, the experimental value of the channeling length coincides with the calculated value within error bar.

The support of the management and staff at the FRM II, Garching, is gratefully acknowledged. This work was supported by a Focused Neutron Research Funding of the Max Planck Society, Munich. The authors are grateful to J. Franke for the technical help during the experiments.

[1] F. Pfeiffer, V. Leiner, P. Høghøj, and I. Anderson, Phys. Rev. Lett. **88** (2002) 055507.
[2] S.V. Kozhevnikov, A. Rühm, F. Ott, N. K. Pleshanov, J. Major, Physica B **406** (2011) 2463.
[3] V.K. Ignatovich, F. Radu, Phys. Rev. B **64** (2001) 205408.
[4] Y.P. Feng, C.F. Majkrzak, S.K. Sinha, D.G. Wiesler, H. Zhang and H.W. Deckman, Phys. Rev. B **49** (1994) 10814.
[5] S.P. Pogossian, A. Menelle, H. Le Gall, J.M. Desvignes, and M. Artinian, Pys. Rev. B **53** (1996) 14359.
[6] A. Menelle, S.P. Pogossian, H. Le Gall, J. M. Desvignes, J. Ben Youssef, Physica B **234-236** (1997)510.
[7] V.L. Aksenov, Yu.V. Nikitenko, Physica B **297** (2001) 101.

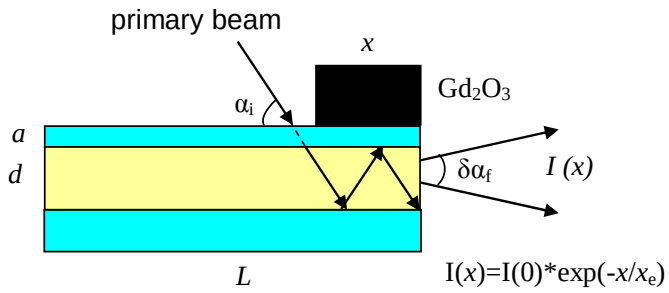

Fig. 1. Geometry of the experiment.

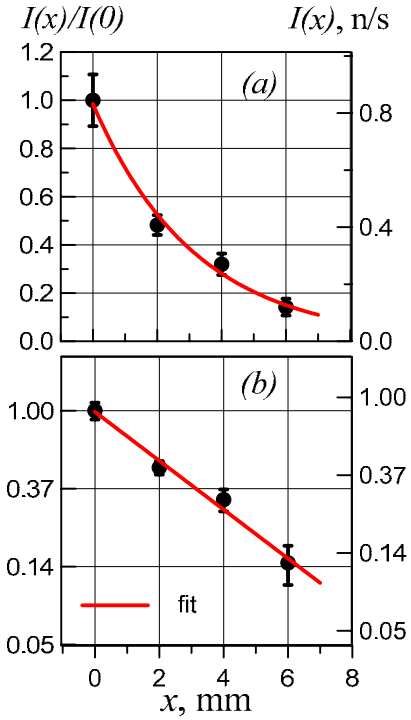

Fig. 2. Integrated microbeam intensity at the resonance angle α_{i0}=0.37° as a function of the Gd_2O_3 powder length.

RIETVELD TEXTURE ANALYSIS OF SKAT DIFFRACTOMETER DATA: RECENT ADVANCES AND PERSPECTIVES

S. Matthies[a], R.N. Vasin[a]

[a] Frank Laboratory of Neutron Physics, Joint Institute for Nuclear Research, 141980, Dubna, Moscow Region, Russia

The texture specialized diffractometer SKAT [1] is located on the beamline 7a of the pulsed fast reactor IBR-2. The rather long (≈ 103.8 m) flight path of the thermal neutrons and the chosen scattering angle of $2\theta = 90°$ permit to investigate lattice spacing in the range of $d \approx 0.6…4.7$ Å, with a resolution of $\Delta d/d \approx 0.55\%$. That is sufficient to study the lattice preferred orientations (LPO) of most rocks and engineering materials. Commonly a finite (usually < 6 for each phase) number of complete experimental pole figures (PF) is used to determine the orientation distribution function (ODF) of the crystallites of the main phases in a sample. The construction of the experimental PFs with a 5ºx5º angular grid (19 detectors and 72 sample positions lead to 1368 spectra) requires the manual selection of intensive non-overlapped diffraction peaks from the TOF diffraction patterns.

This approach has some drawbacks. E.g., in the case of rocks containing several minerals with a low crystal symmetry (such as biotite, albite, orthoclase, etc.), the selection of non-overlapped peaks is often possible (if possible at all) only at high d ranges (e.g., $d > 3.5$ Å), where the counting rates in the SKAT spectra are quite poor. In this case only a small part of the available rich diffraction information in the measured spectra is used. The "Rietveld texture analysis" [2, 3] developed in the last decade permits to analyze many diffraction patterns (even highly peak overlapping regions) as a whole, and, beyond the ODF determination, also to receive some additional information about the sample: phase volume fractions, cell parameters, residual stresses, etc.). The freeware program system MAUD [2-4], utilizing the modified Rietveld method, also possesses a number of options for the determination of the ODFs for multiphase samples from TOF diffraction spectra. Therefore a possibility existed to apply MAUD to the typical set of SKAT spectra. In order to adapt the SKAT data for a MAUD analysis a user-friendly C++-based program SKAT2MAUD has been developed and thoroughly tested during the last year. In future the program may easily be adjusted for the processing of data from other IBR-2 diffractometers like FSD, EPSILON-MDS or new SKAT version with several detector rings. Using MAUD the analysis of conventional SKAT spectra from manifold samples of different type (powders, single-phase polycrystals with LPO, single-phase polycrystals with LPO and residual stresses, multi-phase polycrystals with LPO of each phase) has been performed and showed excellent results.

As an example below some results are presented concerning the texture analysis of biotite in the gneiss samples OKU818 (composed by 39.9 vol.% quartz, 37.4 vol.% andesine plagioclase and 22.6 vol.% biotite) from the Outokumpu scientific drill borehole. Samples of roughly cubic shape cut from the same block have been investigated on the SKAT and HIPPO (Los-Alamos) [5] diffractometers. The data have been processed by MAUD in case of HIPPO (the long been developed routine analysis procedures are described in [3, 5]) and in case of SKAT by two methods: using MAUD and the up to now applied conventional method (analyzing pole figures) described in [6]. In order to compare the derived ODFs with account for the real angular resolution of the diffractometers in the pole figure space the original HIPPO ODF has been smoothed by a Gaussian function in the orientation space with a FWHM = 20° (the HIPPO PF resolution depends on the scattering angles of the detector rings and rises from 10 up to 19° [5]). The original SKAT ODFs have been filtered (with preserving texture sharpness) by a Gaussian function with the FWHM = 7.5° (the mean angular size of the SKAT detectors in the pole figure space of about 3° is much lower than for HIPPO, but the 5ºx5º measuring grid of SKAT reduces its available resolution to effectively 7.5°). The results presented in Table 1 show that the Rietveld texture analysis applied to both diffractometers yields nearly the same results, while the conventional pole figure analysis of the SKAT data (using only some isolated peaks in the TOF spectra) clearly underestimates the

sharpness of the biotite texture. The difference of the f_{min} values (isotropic texture background "phon") for the final HIPPO and SKAT MAUD ODFs is most probably connected with the lower SKAT counting statistics and the corresponding difficulties to correctly estimate and to subtract the background from TOF spectra. Thus, even though the SKAT diffractometer is able to investigate larger samples (in order to achieve a representative grain statistics) and possesses a relatively high angular resolution (necessary to correctly detect sharp orientation distributions), in practice the better counting statistics of the HIPPO diffractometer at LANSCE is very valuable for most quantitative texture studies and allows to perform the measurements in a reasonable time (e.g., the OKU818 measurements have been performed in 8 hours on HIPPO vs. 36 hours on SKAT). This drawback should be overcome with the improved SKAT diifractometer that expected to have a several times higher flux at the sample due to the new neutron guide.

Table 1. Characterization of the biotite ODF in the OKU818 gneiss sample: minimum ODF value f_{min}, maximum ODF value f_{max}, texture index F2, part of non-randomly oriented crystallites SH>1 and the part of orientation space volume occupied by these crystallites CPGs>1.

Instrument (processing)	f_{min}	f_{max}	F_2	SH>1, %	CPGs>1, %
HIPPO (MAUD)	0.03	26.45	6.2	58.5	17
SKAT (MAUD)	0.08	26.88	6.1	53.8	17
SKAT (conventional PF)	0.01	21.05	3.5	44.4	24

Another advantage of the analysis of the SKAT data using MAUD opens additional possibilities for the optimization of future experiments. Due to the use of a great number of diffraction peaks (now including overlapped ones too) the formal number of considered experimental PFs is great. Consequently, only a limited coverage of the experimental PF will be sufficient for the ODF reconstruction preserving the same angular resolution. This infers that it is e.g. possible to perform measurements with less sample orientations than before, drastically reducing the total measurement time for a given sample (for up to 12 times!, cf. Fig.1) and/or simultaneously to increase the counting statistics for each sample position (e.g., measuring only 1/6 of the complete pole figure coverage, but measuring each position for 1.5 hours instead of 0.5 hours).

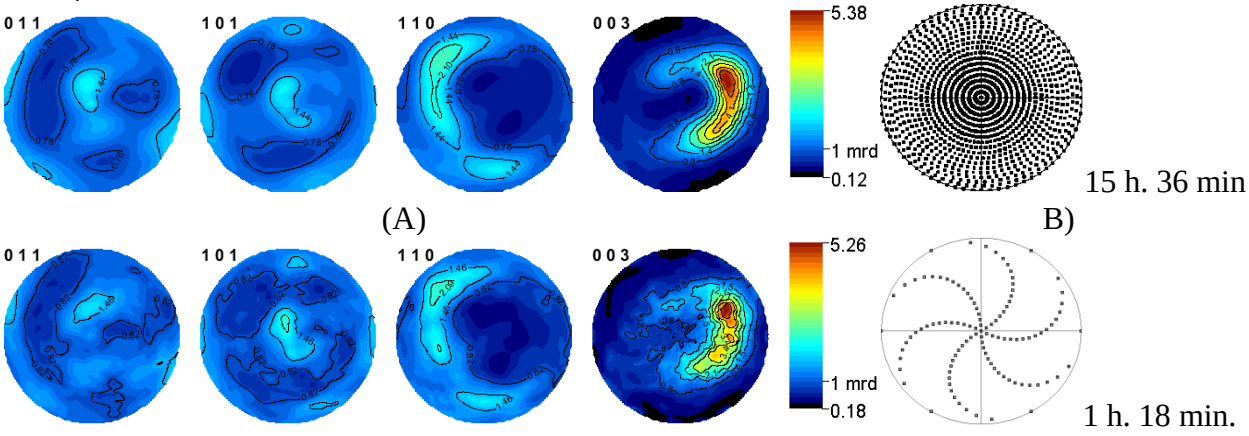

Fig.1. Pole figures of the quartz in the quartzite sample 26a. Equal area projections, linear scale contours. Conventional PF analysis of all data (texture index F2=2.35) (A), corresponding PF coverage and measurement time (B); analysis of 1/12 part of data with MAUD (texture index F2=2.24) (C), corresponding PF coverage and estimated measurement time (D).

1. K. Ullemeyer, P. Spalthoff, J. Heinitz, N.N. Isakov, A.N. Nikitin, K. Weber. The SKAT texture diffractometer at the pulsed reactor IBR-2 at Dubna: experimental layout and first measurements. Nuclear Inst. and Methods in Physics Research A, **412**, 80-88, 1998.

2. L. Lutterotti. Total pattern fitting for the combined size-strain-stress-texture determination in thin film diffraction. Nuclear Inst. and Methods in Physics Research B, **268**, 334-340, 2010.
3. H.-R. Wenk, L. Lutterotti, S.C. Vogel. Rietveld texture analysis from TOF neutron diffraction data. Powder Diffraction, **25**, 283-296, 2010.
4. L. Lutterotti, S. Matthies, H.-R. Wenk. MAUD: a friendly Java program for material analysis using diffraction, IUCr: Newsletter of the CPD, **21**, 14-15, 1999.
5. S. Matthies, J. Pehl, H.-R. Wenk and S. Vogel. Quantitative texture analysis with the HIPPO TOF diffractometer. J. Appl. Cryst., **38**, 462-475, 2005.
6. H. Kern, T.I. Ivankina, A.N. Nikitin, T. Lokajicek, Z. Pros. The effect of oriented microcracks and crystallographic and shape preferred orientation on bulk elastic anisotropy of a foliated biotite gneiss from Outokumpu. Tectonophysics, **457**, 143-149, 2008.

Development of the SESANS spectrometer elements based on rotating magnetic fields

A. Rubtsov[a], A. Ioffe[b], V. Bodnarchuk[a], S. Manoshin[a]

[a]Frank Laboratory of Neutron Physics, Joint Institute for Nuclear Research, Dubna, Russia
[b]Juelich Centre for Neutron Science at FRM-II, Forschungszentrum Juelich, Garching, Germany

The new spin-echo method based on the use of rotating magnetic field was proposed recently [1]. After this there were carried out number of experiments in order to test the idea and estimate the perspectives. In the experiment described here we constructed the prototype of one spin echo arm which consist of two spin flippers with rotated magnetic field (RMF). Magnetic fields in spin-flippers are confined in flipper plane and are rotated in the plane normal the propagation direction, *yz*, of the neutron beam polarized along the vertical *z*-axis (see fig. 1,2). All three components of polarization vector passed through the set up were measured in dependent on the applied current frequency. Experiment was carried out on TREF spectrometer (JCNS) at FRM II reactor.

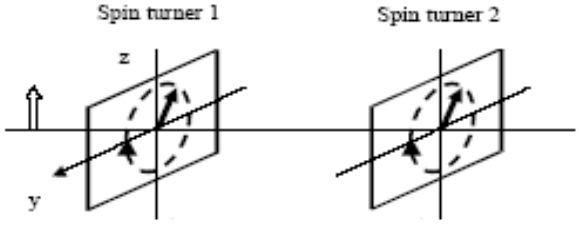

Fig.1 One arm of NSE set-up composed by two spin turners.

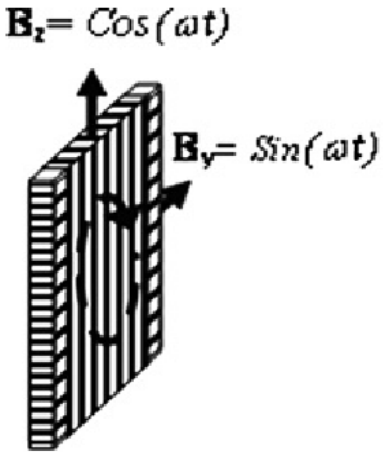

Fig. 2 The spin turners as rectangular electromagnetic coils with two windings perpendicular to each other. Each windings feed by the sinusoidal current with phase shifting of $\pi/2$ between them.

To analyse the behaviour of the neutron spin in such a flipper we calculate the magnetic fields distribution inside and outside of the flipper with use of the MagNet [2] software. Based on the calculated magnetic fields we compare the experimental data on the neutron spin passage through the flippers with simulation of this process in the VITESS [3] package. For this purpose it was updated the VITESS modules using magnetic field. In the new version the magnetic field can be loaded from the external source. This is a great advantage because in previous version magnetic fields configuration can be defined by limited number of parameters and functions. Using of the new option allows taking into account the influence of such factors as border effects, effects of non-

full field shielding and so on. At Fig.3 one can see the experimental dependence of Pz polarization component measured at the exit from the set-up shown at Fig.1 and it's VITESS simulations.

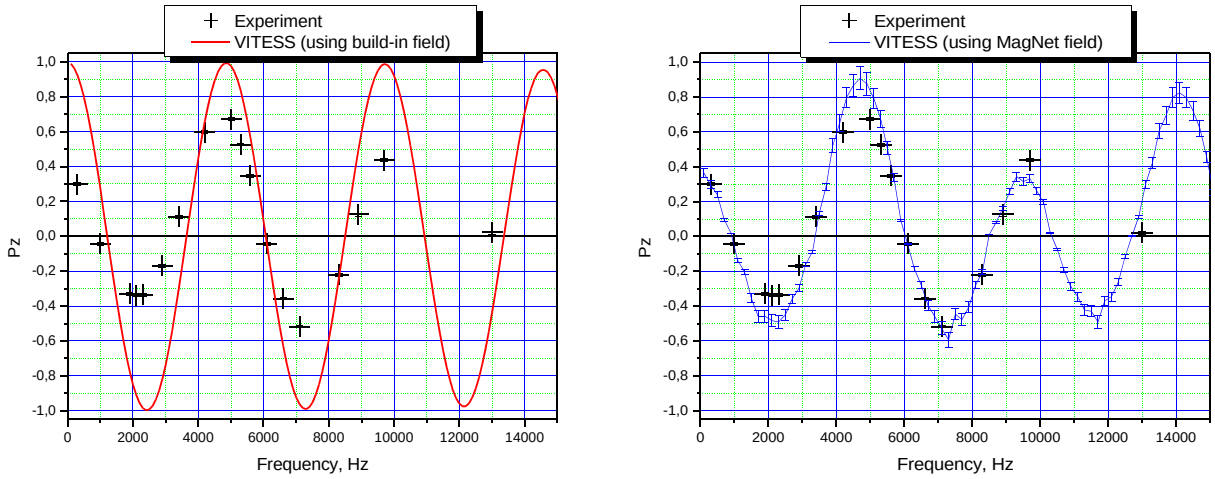

Fig.3 Frequency dependence of the *z*-component of the polarization in compare with VITESS simulation. Solid line on the left picture is simulation with magnetic fields generated in VITESS. Solid line on the right picture is simulation with magnetic fields generated by MagNet.

Thus the cooperative of two software packages gives new possibilities in description of experimental data with passage of neutron polarization through the time-dependent magnetic field configuration. It allows improving the construction of NSE elements and it efficiency.

References

[1] A.Ioffe, Physica **B 335** (2003) 169.
[2] MagNet web site: <http://www.infolytica.com/en/products/magnet/ >.
[3] VITESS web site: <http://www.hmi.de/projects/ess/vitess>.

NEUTRON AND SYNCHROTRON X-RAY DIFFRACTION STUDY OF MODEL ORAL STRATUM CORNEUM LIPID MIXTURES

N.Yu. Ryabova[a, b], A.Yu. Gruzinov[c], A.V. Zabelin[c], S.G. Sheverev[a], A. Buchsteiner[d], T. Haußd[d]

[a]Joint Institute for Nuclear Research, 141980, Dubna, Moscow Reg., Russia
[b]Skobeltsyn Institute of Nuclear Physics, Moscow State University, 119992, Moscow, Russia
[c]National research center "Kurchatov Institute", 123182, Moscow, Russia
[d]Helmholtz-Zentrum Berlin für Materialien und Energie, 14109, Berlin, Germany

The epithelium covering the oral cavity (oral stratum corneum, OSC) provides a protective barrier for underlying tissue, but it is not so distinct like the epidermal stratum corneum (ESC). The OSC lipid matrix consists mainly of the phospholipids (PL), cholesterol (Ch), fatty acids (FA), cholesterol sulphate (ChS), triglycerides and short-chain ceramides (CERs). Although the lipid composition of the OSC is well defined the physical studies of the nanostructure of rare OSC-lipid bilayers are lacking [1] and their role in formation of the barrier function is still unclear. Neutron and X-ray diffraction experiments have been performed to characterize the structure of model OSC lipid mixtures.

The model lipid mixtures CER6/Chol/FA/ChS/PL = 28/23/15/8/26 (w/w) with individual fatty acids (FA) have been studied. To prepare the samples the $SM_{bovine\ brain}$, DPPC, DPPE (PL=SM/DPPC/DPPE=1/2/1 m/m), CER6, Ch, ChS, palmitic acid (PA, C16:0), stearic acid (SA, C18:0), arachidic acid (AA, C20:0), behenic acid (BE, C22:0), and lignoceric acid (LA, C24:0) and their mixture FFA =SA/AA/BA/LA = 29/21/15/8/26 (w/w) have been used. Neutron diffraction experiment on the oriented samples has been carried out on the V1 membrane diffractometer, located at cold-neutron source of the BER-II research reactor (BENSC, HZB), with a neutron wavelength of 5.23 Å and a sample-to-detector distance of 102.52 cm. Small-angle-X-ray diffraction patterns from multilamellar vesicles (MLVs) have been collected on the small angle time resolved station DICSI at the K1.3a beamline of the Siberia-2 storage ring of the Synchrotron Radiation Source at the NRC "Kurchatov Institute".

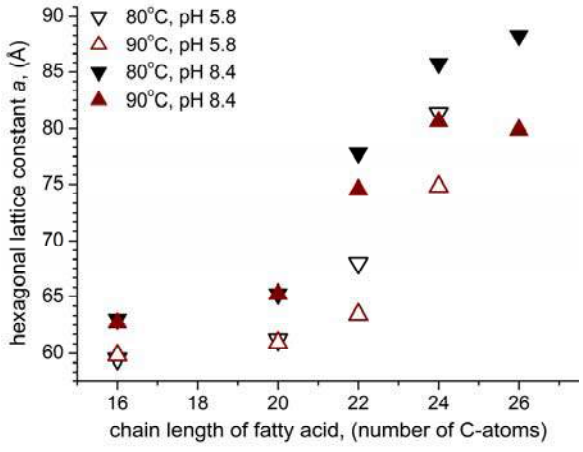

Fig. 1. The lattice parameter of the inverted hexagonal phase H_{II} as a function of hydrocarbon chain length of fatty acid for the membranes CER6/Chol/FA/ChS/PL at 80 and 90°C.

MLVs of OSC-model mixtures with PA, AA are characterized by presence of two lamellar phases with repeat distance of 46.4 and 42.2-43.8 Å in the temperature range of 20-37°C, at pH 5.8 and 8.4. At the same conditions the lipid mixtures with LA, BA and CA have a dominating phase with periodicity of 47-52.9 Å at pH 5.8 and 48.1-61.8 Å at pH 8.4. The inverted hexagonal phase H_{II} coexists with liquid crystalline lamellar phase at the temperature of 80-90°C. The parameter of the H_{II} phase increases with the hydrocarbon chain length of fatty acids and also increases with a change of pH from 5.8 to 8.4 for all lipid mixtures with individual fatty acids (Fig. 1). The lamellar phase of the membranes with long-chain fatty acids (AA, LA, BA and CA) is suppressed at pH 8.4.

The oriented membrane CER6/Chol/FFA/ChS/PL is characterized by coexistence of several structure phases. The main phase with repeat distance $d \sim 55$ Å at 98% relative humidity (phase "a" at Fig. 2) and the minor phase with $d \sim 58$ Å (phase "d") are likely phospholipids-enriched phases. The low swelling phase with repeat distance $d \sim 44$ Å at 58% relative humidity and $d \sim 46$ Å at 98% relative humidity (phase "b" at Fig. 2) has the structure similar to that of ESC-model membrane, first described in [2].

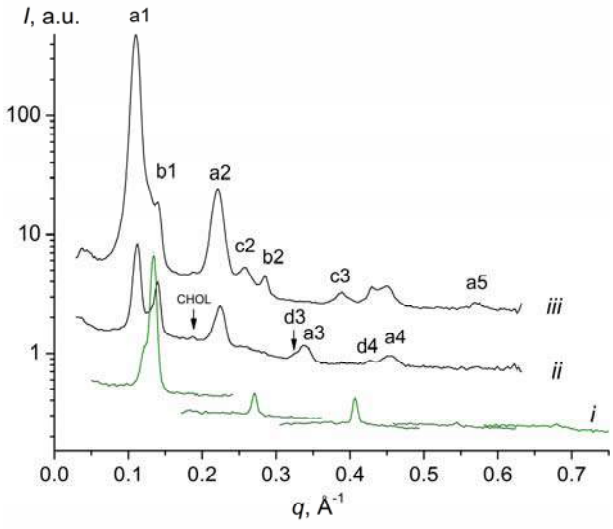

Fig. 2. Neutron diffraction patterns of oriented membrane CER6/Chol/FFA/ChS/PL = 28/23/15/8/26 (w/w) measured at 20°C, 58% RH, D_2O/H_2O = 8/92 (i), 37°C, 98% RH, D_2O/H_2O = 8/92 (ii) and 37°C, 98% RH, D_2O/H_2O = 80/20 (iii). Numbers indicate the diffraction orders for phases "a", "b", "c" and "d".

Earlier, electron microscopy revealed an inverse correlation between permeability and ceramide content for both skin and oral tissues [3]. One can suppose that there are some ceramides-rich domaines in the native oral lipid material, which responsible for control of permeability.

References

1. P.W. Werzt, B. van den Bergh. Chemistry and Physics of Lipids 91. 1998. 85-96.
2. Kiselev M.A., et.al. European Biophysics J. 34. 2005. 1030-1040.
3. Law, S., et.al. Arch. Oral Biol. 40. 1995. 1085–1091.

ISOTHERMAL COMPRESSIBILITY AND THICKNESS OF LIPID BILAYER SIMULTANEOUSLY MEASURED UNDER HYDROSTATIC PRESSURE

Soloviov D.V., Ivankov O.I., Gorshkova Yu.E., Petuhova T.B., Kovalev Yu.S., Sirotin A.P., Gordeliy V.I. † and Kuklin A.I.†
FLNP JINR
E-mail: † kuklin@nf.jinr.ru; valentine.gordeliy@ibs.fr

Soloviov D.V., Ivankov O.I.
Taras Shevchenko National University of Kyiv, Ukraine

Gordeliy V.I.
Institute of Structural Biology J.P.Ebel, France
Institute of Complex System- 5, Germany

Gordeliy V.I. and Kuklin A.I.
Bionanocenter of Moscow Institute for Physics and Technology, Russia

Introduction

The IBR-2M pulsed reactor (JINR, Dubna, Moscow region) was launched in operation in 2011. One of the instruments at the reactor is a YuMO small-angle neutron scattering spectrometer which is used for a wide range of scientific and technical applications.

The spectrometer is characterized by a relatively short data acquisition time which depends on the type of the studied material and varies from minutes to hours. In case of the results of the studies of lipid membranes under hydrostatic pressure which are described below the characteristic time was several minutes due to a high flux of the neutron beam [1]. In addition, the sample environment of the SANS instrument was also improved providing new opportunities for the studies in different fields of science. The neutron experiments were performed at YuMO spectrometer by a two-detector system mode with ring wire detectors [4,5]. The beam was collimated to a diameter of 14 mm on the sample. The data treatment was performed by SAS program [6] both with and without a smoothing mode [7]. In this report we describe a high pressure setup (4 kbar) recently installed at the YuMO [2]. We also present the new SANS D-P-V-T on lipid membranes data obtained simultaneously. It should be mentioned that the first test experiments with P-V-T measurements were done in [3].

Experiment

Synthetic 1,2-dipalmitoyl-sn-glycero-3-phosphocholine (DPPC) was purchased from Avanti (Birmingham, Al) and was used without further purification. Water (18 MV/cm) was obtained with Millipore (USA). Multilamellar vesicles (MLVs) were prepared in the following way: DPPC was mixed with water. Homogeneous dispersion was obtained by a temperature

cycling method around the main phase transition temperature with a temperature range ±20. The final concentration of the lipid/water was 10 mg/ml.

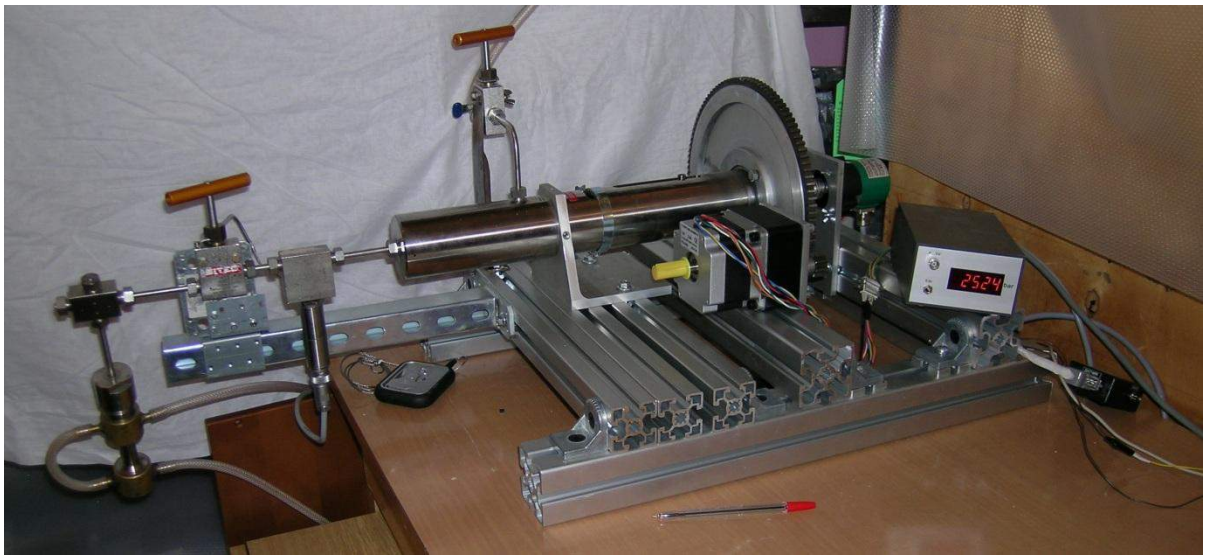

Fig. 1. Volumetric high-pressure setup of the YuMO spectrometer, adapted for SANS experiments.

The hydrostatic high-pressure setup was improved, namely, it was adapted to parallel volumetric measurements. For this purpose the rotation angle sensor was mounted at the hand pressure pump. It provides control of the change of the volume with the accuracy up to $\pm 2*10^{-6}$ ml. In addition, the pressure pump was equipped with a motor which gives a possibility to change the volume of the system at a rate about $2*10^{-3}$ ml/s. The electronic pressure sensor allows one to control pressure with the accuracy of about ± 0,1 bar. The temperature in the pressure cell is controlled by the LAUDA thermostat with an error ± 0,05°C.

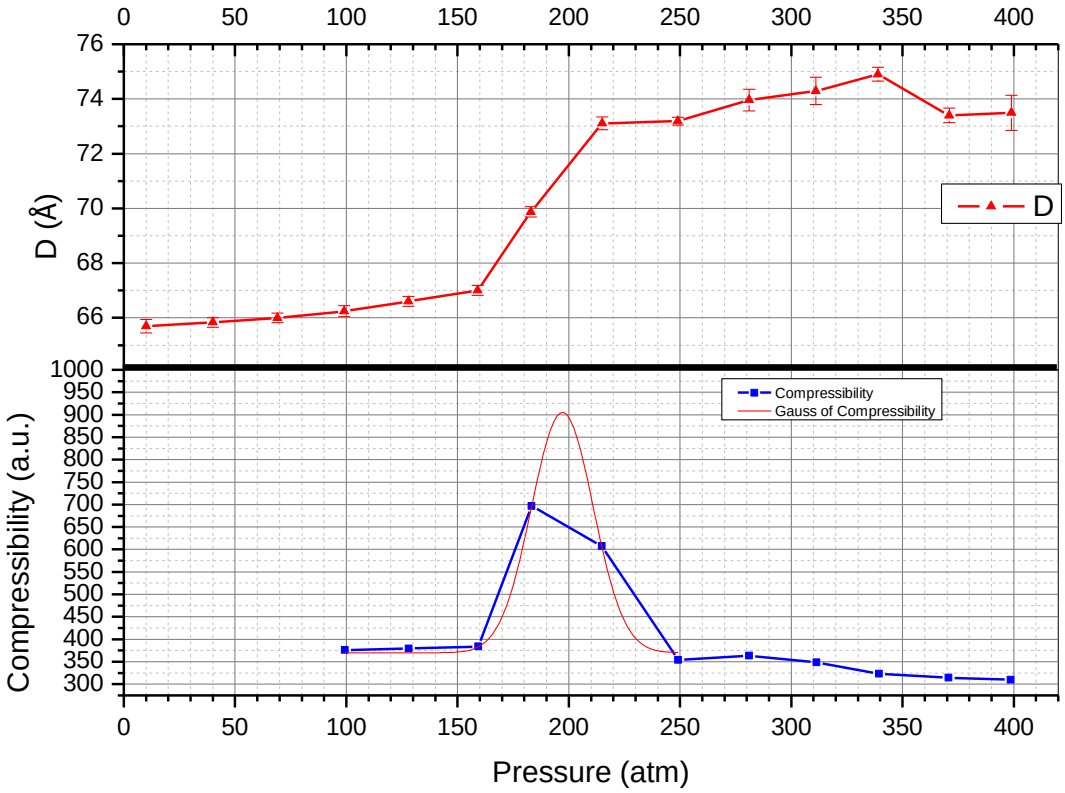

Fig.2. The DPPC main phase transition at 50°C and from 10 to 400 atm range. a) Bilayer repeat distance dependence D vs pressure and b) Membrane isothermal compressibility as the function of pressure.
The measurements were performed simultaneously.

Experimental data on bilayer repeat distance and membrane isothermal compressibility as the function of pressure are presented in Fig.2.

Simultaneous D-P-V-T measurements were done in the following pressure range: from 10 up to 400 atm with a step of 30 atm.

Acknowledgements

The work was supported by the work of Federal Target Program "Scientific and Pedagogical Staff of an Innovative Russia" (state contracts P-1160 and 02.740.11.0542). We are grateful for supporting Seventh Framework Programme [FR7/2007-2013] under grant agreement №211800.

We are grateful to Dr.A.Kh. Islamov for fruitful discussion.

References:

[1] Kuklin A.I., Rogov A.D., Gorshkova Yu. E., Utrobin P. K., Kovalev Yu. S., Rogachev A. V., Ivankov O. I., Kutuzov S. A., Soloviov D. V. and Gordeliy V. I. Analysis of neutron spectra and fluxes obtained with cold and thermal moderators at IBR-2 reactor: Experimental and computer-modeling studies. Physics of Particles and Nuclei Letters. (2011) **8,** 2, pp.119-128.

[2] Kuklin A.I., Soloviov D.V., Rogachev A.V., Utrobin P.K., Kovalev Yu.S., Balasoiu M., Ivankov O.I., Sirotin A.P., Murugova T.N., Petukhova T.B., Gorshkova Yu.E., Erhan R.V., Kutuzov S.A., Soloviev A.G., Gordeliy V.I. New opportunities provided by modernized small-angle neutron scattering two-detector system instrument (YuMO). Journal of Physics: Conference Series. (2011) **291,** 012013, pp.1-7.

[3] Solov'ev D.V., Kuklin A.I., Utrobin P.K., Ozerin A.N., Kurkin T.S., Ivan'kov O.I., Bulavin L.A. and Gordeliy V.I. X-ray scattering and volumetric P-V-T studies of the dimyristoylphosphatidylcholine-water system. Journal of Surface Investigation: X-ray, Synchrotron and Neutron Techniques. (2011) **5**, 1, pp.7-10.

[4] Kuklin A.I., Islamov A.Kh. & Gordely V.I. 'Scientific Reviews: Two-Detector System for Small-Angle Neutron Scattering Instrument', *Neutron News,* (2005) **16:3**, pp.16-18

[5] Kuklin A.I., Islamov A.Kh., Kovalev Y.S., Utrobin P.K. & Gordely V.I. Optimization two-detector system small-angle neutron spectrometer YuMO for nanoobject investigation, Journal of Surface Investigation: X-ray, Synchrotron and Neutron Techniques. (2006) **6,** pp.74-83

[6] Soloviov A.G. et al. The Package for Small-Angle Neutron Scattering Data Treatment. Communication of JINR **P10-2003-86**, JINR, Dubna, 2003.

[7] Soloviev A.G., Litvinenko E.I., Ososkov G.A., Islamov A.Kh., Kuklin A.I. Application of wavelet analysis to data treatment for small-angle neutron scattering, Nuclear Inst. and Methods in Physics Research, A. (2003) **502/2-3,** pp.498-500.

STRUCTURE OF CLUSTERS IN AQUEOUS DISPERSIONS OF NANODIAMONDS BY SMALL-ANGLE NEUTRON SCATTERING: EXPONENTIAL/POWER-LAW APPROACH

O.V. Tomchuk[a,b], L.A. Bulavin[b], V.M. Garamus[c], V.L. Aksenov[d], M.V. Avdeev[a]

[a]*Frank Laboratory of Neutron Physics, JINR, Dubna, Russia*
[b]*Kyiv Taras Shevchenko National University, Kyiv, Ukraine*
[c]*Helmholtz Zentrum Geesthacht, Geesthacht, Germany*
[d]*National Research Centre "Kurchatov Institute", Moscow, Russia*

Detonation nanodiamonds (DND) are formed by an explosion of unbalanced oxygen explosives in the absence of extra sources of carbon. DND particles are nanocrystallites of size 5–10 nm which, in the course of the explosion, produce almost inseparable aggregates through nondiamond components. Methods of "clarifying" dispersions which depend on grinding of DND in wet conditions have recently being developed [1]. As a result, stable colloid solutions based on various solvents are synthesized in which individual nanoparticles unite into clusters because of high free surface. In [2] a water–nanodiamond system was studied by the small-angle neutron scattering (SANS) method. The fractal structure of clusters was analyzed using an incomplete two-level model [3]. From a qualitative comparison of the scattering curves it was inferred that, when concentrated, the clusters partially penetrate each other. Similarly, qualitative comparison allowed for an analysis of changes in the scattering curves at different relations between the proton and deuterium components of the buffer (contrast variation), which, within uniform approximation, allowed for the estimation of the composition of the clusters.

The aim of the present work was to simultaneously study the fractal structure of nanodiamond clusters and the effect of cluster interaction, based on a complete two-level model [3]. We used SANS curves obtained at the SANS-1 small-angle diffractometer in HZG (Geesthacht, Germany). In the SANS curves for different solution concentrations (Fig.1a), we observe two power-law regions, which in the double logarithmic scale are linear, and the Guinier regime is observed in the small-q range. The scattering represents the two-level organization of particles in an aqueous suspension of DND: the cluster level and the level of nanodiamond particles. The power character of the curves in the first level (small q) suggests that the studied system exhibits fractal properties [4]. The curves were described within the framework of a universal exponential/power-law approach (Fig.1b) [3] (for notation see Ref.2).

From the derived value of the index $P = 2.4 < 3$, it follows that the organization of the nanodiamond particles in aggregates corresponds to mass fractals with dimension $D = P$, which is independent of DND concentration. The latter implies that the power decrease amplitude in the cluster level (B) depends only on the nanodiamond particles content of dispersion [4]. The D value points to the mechanism of the cluster–cluster aggregation limited by diffusion at the formation of the studied aggregates [5]. The index value in the other level $P_S = 4.2 > 4$ gives an indication of the so-called diffusion character of the surface of DNDs making up the aggregates [4]. The initial section of the spectrum gives the apparent radius of gyration R_g. At low concentrations (weak interaction between clusters), it corresponds to the cluster size. For uniform particles of spherical shape, the particle radius is related to R_g as $R=(5/3)^{1/2}R_g$, hence we arrive at the cluster size estimate at a level from 35 to 50 nm. The observed R_g of aggregates first increases with DND concentration (Fig.1b), which efficiently corresponds to a rather strong attraction component in the potential of cluster interaction. At the same time, from analysis of scattering into a zero angle G we draw a conclusion about the general repulsion of clusters, which coincides with qualitative analysis in [2]. The same is true, for example, for the interaction of free monocarbon acids in liquid colloid solutions of magnetic nanoparticles [6]. At concentrations over 5 wt % the radius of gyration begins to decrease and becomes smaller than the initial R_g at the lowest concentration. This indicates that the effective radius of interaction grows smaller than the cluster radius and agrees with the

conclusion about the partial overlapping of branched clusters [2]. The other quantities G_S, B_S increase linearly with concentration, accounting for the increase of DND particles in the solution.

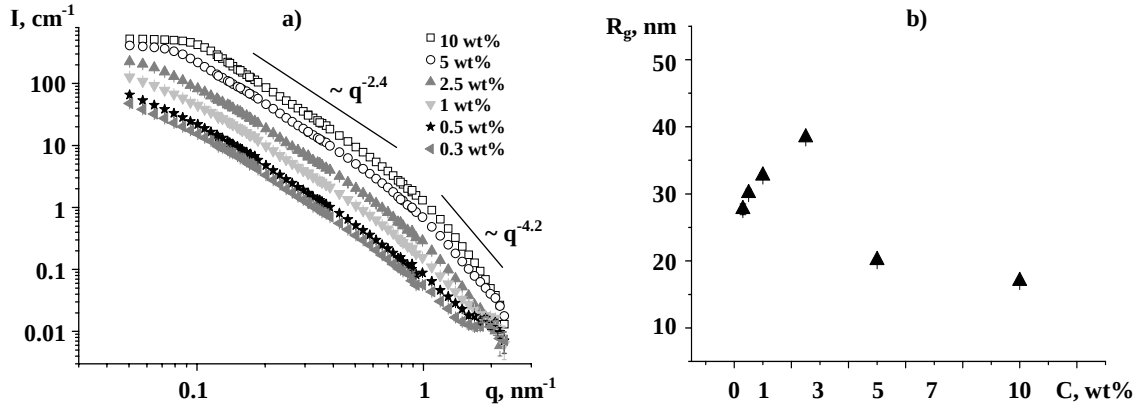

Fig.1. (a) SANS curves from DND water dispersions at different concentrations; (b) concentration dependences of the R_g-parameter.

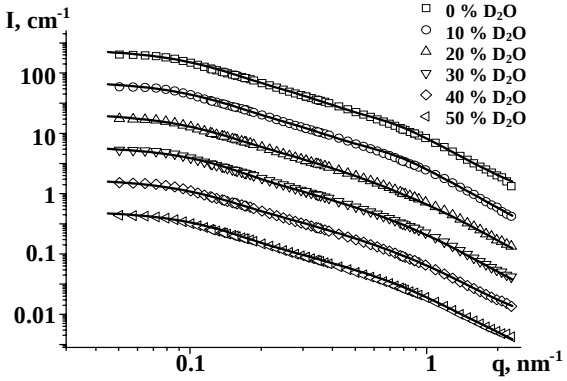

Fig.2. Contrast variation for a water–DND liquid system. For convenience of perception, the intensities are divided by: 10 for the system 10% D_2O; by 100 for the system 20% D_2O; by 1000 for the system 30% D_2O; by 10000 for the system 40% D_2O; by 100000 for the system 50% D_2O. Solid curves are approximations of exponential/power-law model.

The contrast variation procedure (Fig.3) allowed us to find the match point of the aggregates. The obtained value of the scattering length density is smaller than that of crystal diamond (ρ_{CD} = 11.8(3) × 10^{10} cm^{-2}), suggesting the presence of a non-diamond component in the DND particle composition. Since amorphous carbon and noncarbonic admixtures are almost entirely removed from the surface of nanodiamond particles during the preparation of dispersion [1], we may suggest that around the diamond's core there is a graphene shell, which is responsible for the diffusion character of the DND surface. The existence of such a shell follows from the spectroscopic data [2,7]. Also, the decrease of R_{gS} with contrast from 4.6(8) to 2.8(5) nm is consistent with this conclusion, because the shell is partially shaded from the scattering viewpoint as the share of heavy water in the buffer increases. Scattering decays monotonically with increasing deuterium component content of the buffer, P is invariant to contrast, which is evidence for the homogeneity of the aggregates under study.

References

[1] E. Osawa, Pure Appl. Chem. **80**, 1365 (2008).
[2] M.V. Avdeev et al., J. Phys. Chem. C **133**, 9473–9479 (2009).
[3] G. Beaucage, J. Appl. Cryst. **29**, 134–149 (1996).
[4] P.W. Schmidt, J. Appl. Cryst. **24**, 414–435 (1991).
[5] R. Vacher, T. Voignier, J. Pelous, and E. Courtens, Phys. Rev. B **37**, 6500-6503 (1988).
[6] V.I. Petrenko, et al., Solid State Phenom. **152–153**, 198–201 (2009).
[7] S. Osswald, et al., Am. Chem. Soc. **128**, 11635 (2006).

STUDY OF C_{60}/NMP/TOLUENE AND C_{60}/NMP/WATER SOLUTIONS BY UV-VIS SPECTROSCOPY AND SMALL-ANGLE NEUTRON SCATTERING

T.V. Tropin[a], T.O. Kyrey[a,b], O.A. Kyzyma[a,b], A.V. Feoktistov[c], M.V. Avdeev[a], L.A. Bulavin[b], L. Rosta[d], V.L. Aksenov[e,a]

[a]*Frank Laboratory of Neutron Physics, JINR, Dubna, Russia*
[b]*Kyiv Taras Shevchenko National University, Kyiv, Ukraine*
[c]*Forschungszentrum Jülich, Jülich, Germany*
[d]*Research Institute for Solid State Physics and Optics, Budapest, Hungary*
[e]*National Research Centre "Kurchatov Institute", Moscow, Russia*

Solutions of fullerene C_{60} in nitrogen-containing solvents and their mixtures with other solvents are characterized by the evolution of their UV-Vis, IR and Raman spectra in time. Two main processes, namely the formation of C_{60} clusters and change in the solute-solvent interaction, contribute to these phenomena [1,2]. These solutions exhibit sharp solvatochromism (change in the UV-Vis spectrum) under slight variations either the fullerene concentration or the solvent composition. Particularly, the addition of highly polar water with dielectric constant $\varepsilon \sim 80$ to the solutions of C_{60} in N-methyl-2-pyrrolidone (NMP) with $\varepsilon = 32$ is accompanied by a specific increase in the absorbance over the wavelength range of 450-550 nm [3-7]. It is supposed that this change in the UV-Vis spectrum is a result of the formation of charge transfer complexes between C_{60} and H_2O. Since NMP is miscible with both high-polarity (such as water) and low-polarity (such as toluene) solvents this later statement can be carefully checked. In the given work we studied the absorbance characteristics and structure of the solution of fullerene C_{60} in the mixtures NMP/toluene and NMP/water obtained by adding the third component to the initial C_{60}/NMP solution. For this purpose the combination of UV-Vis spectroscopy and small-angle neutron scattering (SANS) was used.

Fullerene C_{60} was dissolved in NMP with stirring during 15 minutes at room temperature. The initial mauve color of the solution after the preparation turned to brownish-yellow with time. Ternary solutions C_{60}/NMP/toluene and C_{60}/NMP/water were obtained by adding the third components to C_{60}/NMP with various proportions in different times after the preparation of the initial solution. Absorption spectra were obtained at the Hitachi U-2000 UV-Vis spectrophotometer in a wavelength range of 200-1000 nm. SANS experiments were carried out the 'Yellow Submarine' set-up of the Budapest Neutron Center.

UV-Vis spectra of C_{60}/NMP and C_{60}/NMP/toluene solutions are compared (Fig.1*a*) in the range of 300-600 nm, where the main specific changes take place. Particularly, they concern the characteristic peak at $\lambda \sim 330$ nm, for which the toluene addition to C_{60}/NMP system is accompanied by a small bathochromic effect (see inset to Fig.1*a*) with a maximal shift of about 4 nm towards higher wavelengths in the limiting case (toluene content of 98 vol. %).

The discussed spectrum region changes considerably when the toluene content exceeds 95 vol. %, so one can talk about a sharp solvatochromism implying somewhat a transfer from C_{60}/NMP to C_{60}/toluene absorption spectrum. However, even at the high content of toluene the color of C_{60}/NMP/toluene solution remains brownish yellow, which is a typical feature of the pure C_{60}/NMP solution. The observed effect is compared (Fig.1*b*) with the solvatochromism occurred at the addition of water to the C_{60}/NMP system, where the bathochromic shift of the peak at $\lambda \sim 330$ nm is about ten times larger than in C_{60}/NMP/toluene. Also, some additional absorption bands (plateau) in the range of 450-600 nm appear. All this points out a specific interaction of water with fullerene dissolved *first* in NMP. The observable changes in the character of the spectrum at the water addition take place at significantly lower water content (around 50 vol. %) [5-8] as compared to toluene. The same threshold of the water content was reported for the similar system C_{60}/pyridine/water [4].

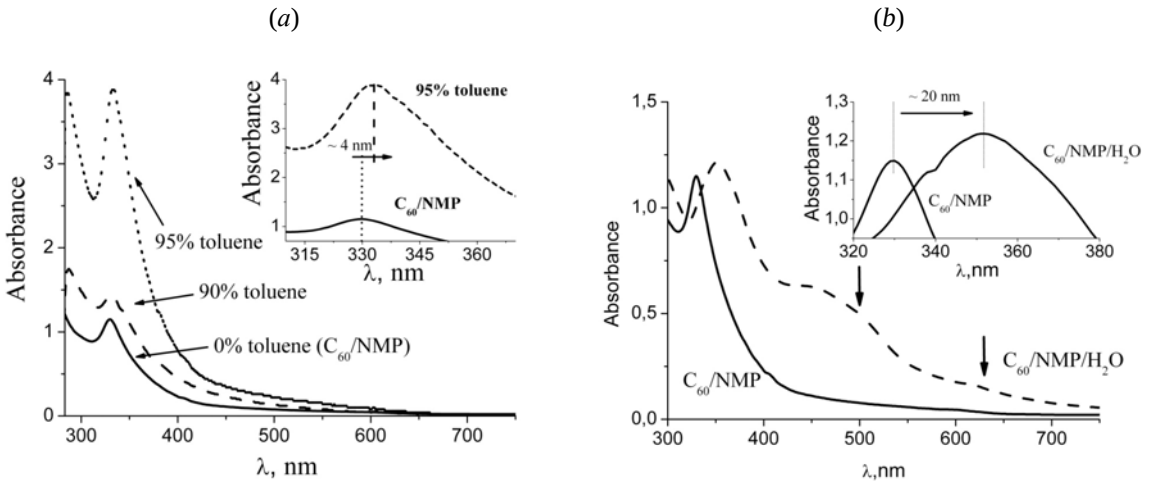

Fig.1. Solvatochromism under addition of toluene (*a*) and water (*b*) to C_{60}/NMP in various proportions. Final volume fractions of toluene in the mixtures are indicated in the graph. Water is added in 50 vol. %. Insets show bathochromic effects for characteristic peak at λ ~ 330 nm. Arrows denote newly appeared absorption bands in case of water addition.

The found difference in the effects of low-polar and polar additives can be related to the solvation processes. Toluene, as a low-polar component in C_{60}/NMP/toluene system, increases the so-called selective solvation, when C_{60} is preferably surrounded by NMP molecules. The corresponding solvation shell starts to be destroyed only at the toluene content close to pure C_{60}/toluene solution. Vice versa, at the water addition the interaction of C_{60}–NMP favours the formation of either the new complexes C_{60}–H_2O, which do not appear, if fullerene is added directly to water, or mixed solvation shells C_{60}–NMP/H_2O.

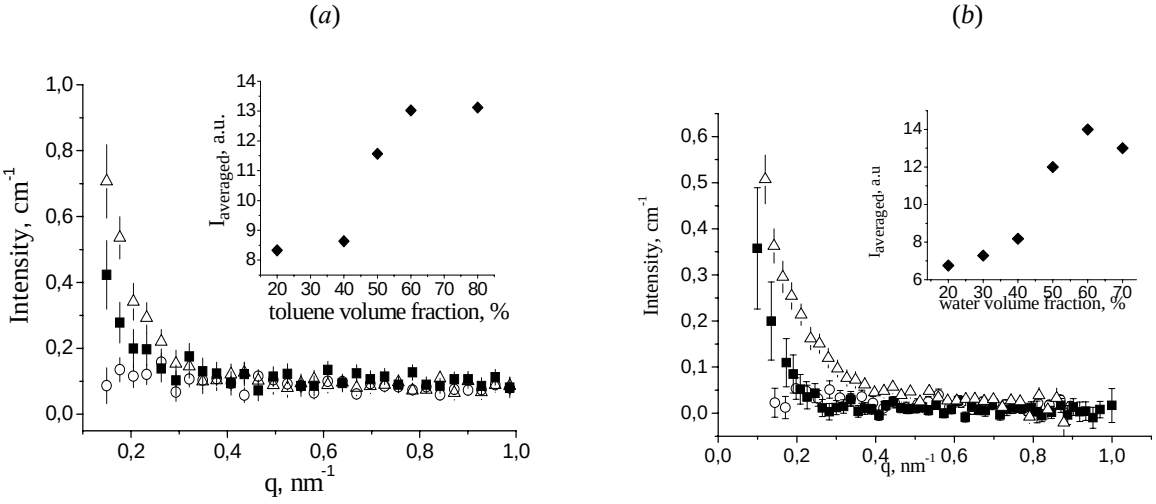

Fig.2. SANS data for C_{60}/NMP/toluene (a) and C_{60}/NMP/water (b) at various content of the third component in solutions. The curves are reffered to one fullerene concentration. Insets show dependence of the averaged intensity (q-range of 0.1-0.5 nm^{-1}) on the volume fraction of the third component.

At the same time, the small-angle neutron scattering (SANS) experiments (Fig.2) do not show any principal differences between toluene and water regarding the cluster reorganization in sufficiently old solutions. In both cases there is observed a sharp increase in the SANS intensity after the additive volume fraction becomes more than 40 % in the mixture. Such increase is explained by partial dissolution of the large (size above 100 nm) initial clusters whose preferable size lies after that in the region of nanolevel (10-100 nm). This means that the obsevred

solvatochromism in the studied solutions is not determined by the cluster reorganization, but is a consequence of the change in the donor-acceptor complexes of C_{60} with solvents.

The work was supported by the RF President grant MK-1055.2011.2.

References

[1] Avdeev, M.V., Aksenov, V.L., and Tropin, T.V. (2010) Rus. J. Phys. Chem. A, 84: 1273–1283.
[2] Kyzyma, O.A., Korobov, M.V., Avdeev, M.V., Garamus, V.M., Snegir, S.V., Petrenko, V.I., Aksenov, V.L., and Bulavin, L.A. (2010) Chem. Phys. Lett., 493: 103–106.
[3] Kyzyma, O.A., Korobov, M.V., Avdeev, M.V., Garamus, V.M., Petrenko, V.I., Aksenov, V.L., and Bulavin, L.A. (2010) Fullerenes Nanotubes Carbon Nanostruct., 18: 458–461.
[4] Scharff, P., Risch, K., Carta-Abelmann, L., Dmytruk, I.M., Bilyi, M.M., Golub, O.A., Khavryuchenko, A.V., Buzaneva, E.V., Aksenov, V.L., Avdeev, M.V., Prylutskyy, Y.I., and Durov, S.S. (2004) Carbon, 42: 1203–1206.
[5] Kyzyma, O.A., Bulavin, L.A., Aksenov, V.L., Avdeev, M.V., Tropin, T.V., Korobov, M.V., Snegir, S.V., and Rosta, L. (2008) Materials structure, 15: 17–20.
[6] Aksenov, L., Avdeev, M.V., Tropin, T.V., Korobov, M.V., Kozhemyakina, N.V., Avramenko, N.V., and Rosta, L. (2006) Physica B, 385–386: 795–797.
[7] Aksenov, V.L., Avdeev, M.V., Kyzyma, O.A., Rosta, L., and Korobov, M.V. (2007) Cryst. Rep., 52: 479−482.
[8] Mrzel, A., Mertelj, A., Omerzu, A., Copia, M., and Mihailovic, D. (1999) J. Phys. Chem. B., 103: 11256−11260.

UPGRADE OF THE NEUTRON OPTICAL SYSTEM FOR THE DIFFRACTOMETERS EPSILON-MDS AND SKAT AT THE REACTOR IBR-2

K. Walther[a], Ch. Scheffzuek[a,b], F. Schilling[a], A. Frischbutter[c], A.P. Bulkin[d], V.A. Kudryashov[d], V.V. Shuravlev[b], and A.V. Belushkin[b]

[a]Karlsruhe Institute of Technology, Institute of Applied Geosciences - Petrophysics, Adenauerring 20b, 76131 Karlsruhe, Germany
[b]Frank Laboratory of Neutron Physics, JINR Dubna, 141980 Dubna, Russia
[c]Helmholtz Centre Potsdam, GFZ German Research Centre for Geosciences, Telegrafenberg, 14473 Potsdam, Germany
[d]Petersburg Institute for Nuclear Physics, 188300 Gatchina, Russia

At beam line № 7 of the reactor IBR-2 were situated two diffractometers EPSILON-MDS and SKAT and the spectrometer for inelastic neutron scattering NERA. Both diffractometers EPSILON-MDS and SKAT have shared a common neutron guide with a section of 50 mm × 170 mm (w × h) and stood out due to a long flight path of more than 100 metres. The large cross section of the neutron beam was virtually split into two equal parts — the upper one provided the texture diffractometer SKAT with neutrons, the lower one served the strain diffractometer EPSILON-MDS.

It became evidently that this resolution had some drawbacks. Due to the close distance between this diffractometers and the weak shielding strong scatterer on the sample table of one diffractometer had generated a noticeable background for the other diffractometer.

During the shut down of the reactor the neutron-optical system of these diffractometers has been renewed: Instead of one straight guide two bent guides have been built. The set-up of the neutron guide system is finished. In the meantime the decision was made to renew the neutron guide for the spectrometer NERA, too. This should be done by the end of the year 2011 and then the diffractometers can be mounted at their new sides.

This is to introduce the new neutron optical system for the diffractometers EPSILON-MDS and SKAT. Between two pulses the reactor generates delayed neutrons from the fission during the power pulse and neutrons from the so-called satellites. All these neutrons do not obey any time correlations and can be seen as background. In order to reduce this background there is a background chopper installed at a small distance from the surface of the moderator, *i.e.* at a distance of 5.5 m.

The background chopper is a disk chopper rotating synchronously with the main reflector of the reactor, *i.e.* with a frequency of 5 Hz. Because there are three neutron guides the transparent part of the disk is calculated to be optimally with 60°. The diameter of the disk is 1205 mm. The cover sheets are made from a Ni-steel-alloy but the main part is a carcass made from an Al-alloy. The carcass is filled with bricks of sintered TiH_2 and a small amount of BC_4 (3 mass-%). The thickness of the disk is 100 mm.

Neither Ti nor H is a strong absorber but hydrogen has a rather high incoherent cross section. Therefore the attenuation of the beam is due "scattering out" the neutrons of their flight path. The background chopper maintains a wavelength band for the diffractometer EPSILON-MDS up to 14 Å, but due to frame overlap this band is limited to 7.2 Å.

Directly behind the background chopper starts the neutron guide splitter. The splitter has an overall length of 14 m and includes two channels of dimensions of 50 mm × 95 mm (w × h) and one channel with dimensions of 50 mm × 160 mm (w × h) cross section. Inside the splitter the neutron

guides are straight. In order to get a distance of minimum 1200 mm between the facilities at the end of the flight path the axis of the guide for NERA is inclined by -0.08° to the symmetry axis of the beam. The inclination of the guides for SKAT and EPSILON-MDS is +0.8° and 1.5°, respectively.

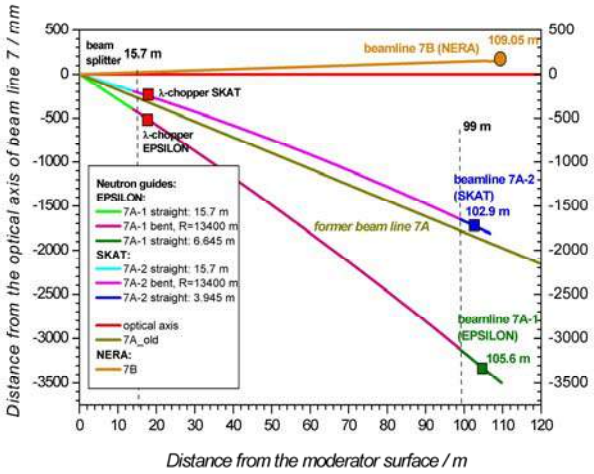

Fig. 1 (left): *Set-up of the neutron guide system at beamline 7 of the pulsed source IBR-2M.*

Fig. 2 (right): *Neutron guide system at beamline 7: 7A-1 (yellow) for the strain diffractometer Epsilon-MDS, 7A-2 (blue) for the texture diffractometer SKAT and 7A-2 (green) for the inelastic spectrometer NERA.*

For a flight path of 105 m the minimal velocity of neutrons is 525 m/s or the corresponding wavelength 7.54 Å for travelling from the moderator to the sample and detector within one frame between two pulses. These facts limit the measurement of peaks with lattice spacing up to 5.33 Å at angles of 2θ= 90°. For instance, many feldspar minerals have large unit cells and therefore they show diffraction peaks beyond this limit.

A frame overlapping can be avoided by suppressing every second power pulse. By this way, a doubling of the wavelength band can be achieved, but the intensity will be also reduced by 50 %. At the distance 22.5 m (EPSILON-MDS) and 25.6 m (SKAT) from the surface of moderator are installed additional choppers of drum-type. If needed, they are switched on and rotate with 150 rpm, *i.e.* the half of the frequency of the rotating main reflector.

After the splitter the neutron guides for both diffractometers are bent with a radius of 13 400 m and the bent part has a length of 85 m. This means, that the exit window of the neutron guide is shifted for 100 mm in respect with a straight guide. The last parts of the guides are straight again in order to get a more homogeneously neutron distribution at sample position.

Acknowledgements
The project has been supported by the German Federal Ministry of Education and Research (BMBF) under contract number 05K09CPA and the Frank Laboratory of Neutron Physics at JINR Dubna.